CHALMERS
UNIVERSITY OF TECHNOLOGY

Nonlinear Bayesian Filtering for Road Geometry Estimation Using Multi-Source Observations

A clothoid-based sensor fusion approach for road geometry estimation using road features, map data, and vehicle trails

Master's thesis in Systems, Control and Mechatronics

Carl Henrysson
Filip Elster

DEPARTMENT OF ELECTRICAL ENGINEERING
CHALMERS UNIVERSITY OF TECHNOLOGY
Gothenburg, Sweden 2026
www.chalmers.se

Master's thesis 2026

Nonlinear Bayesian Filtering for Road Geometry Estimation Using Multi-Source Observations

A clothoid-based sensor fusion approach for road geometry estimation using road features, map data, and vehicle trails

Filip Elster
Carl Henrysson

CHALMERS
UNIVERSITY OF TECHNOLOGY

Department of Electrical Engineering
Division of Systems and Control
Chalmers University of Technology
Gothenburg, Sweden 2026

Nonlinear Bayesian Filtering for Road Geometry Estimation Using Multi-Source Observations
A clothoid-based sensor fusion approach for road geometry estimation using road features, map data, and vehicle trails

FILIP ELSTER
CARL HENRYSSON

Supervisor: Valdemar Krona, Volvo TTI & Agneta Sjögren, Volvo TTI
Examiner: Nikolce Murgovski, Department of Electrical Engineering

Master's Thesis 2026
Department of Electrical Engineering
Division of System and Control
Chalmers University of Technology
SE-412 96 Gothenburg
Telephone +46 31 772 1000

Cover: Volvo Truck illustrating Pilot Assist.

Typeset in LaTeX
Printed by Chalmers Reproservice
Gothenburg, Sweden 2026

Nonlinear Bayesian Filtering for Road Geometry Estimation Using Multi-Source Observations
A clothoid-based sensor fusion approach for road geometry estimation using road features, map data, and vehicle trails
FILIP ELSTER
CARL HENRYSSON
Department of Electrical Engineering
Chalmers University of Technology

Abstract

A nonlinear Bayesian filtering framework is proposed for robust road geometry estimation in Advanced Driver Assistance Systems (ADAS). The method is designed for challenging driving conditions in which conventional road feature detection is unreliable, such as snow-covered roads and degraded or occluded lane markings. The road ahead is represented as a sequence of connected clothoid segments, and recursive state estimation is performed using an Extended Kalman Filter (EKF) for prediction and a Cubature Kalman Filter (CKF) for measurement updates. The framework combines information from multiple onboard sensors and digital map data. The considered measurement sources include lane markings, road edges, barriers, map data, and surrounding vehicle trajectories. Vehicle trails are incorporated through a clothoid-fitting procedure, and statistical gating based on the Normalized Innovation Squared (NIS) is used to reject inconsistent observations. In addition, an adaptive segmentation strategy based on map data information is proposed to improve the alignment between the road representation and the underlying road geometry. The proposed framework is evaluated using recorded vehicle data from highway and snow-covered rural driving scenarios. The results show that the inclusion of map data and surrounding vehicle observations improves estimation accuracy, particularly at longer look-ahead distances. The results further show that the framework maintains a stable estimate of the road centerline even when primary road feature detections are weak or unavailable. Overall, the proposed method demonstrates robust road geometry estimation performance across varying driving environments and highlights the value of combining onboard sensing with map data information.

Keywords: road geometry estimation, clothoid, Bayesian filtering, sensor fusion, Advanced Driver Assistance Systems (ADAS), vehicle trail, map data, Normalized Innovation Squared (NIS)

Acknowledgements

We would like to thank our industry supervisors Valdemar Krona and Agneta Sjögren at Volvo Trucks Technology & Industrial division for their continuous support, guidance, and many valuable discussions throughout the project. We would also like to thank our examiner Nikolce Murgovski at the Department of Electrical Engineering, Chalmers, for valuable feedback and guidance throughout the work. Finally, we would like to extend our gratitude to everyone at Vehicle Environment and Safety at Volvo TTI who contributed in various ways, whether through discussions, feedback, or practical assistance.

Filip Elster & Carl Henrysson, Gothenburg, June 2026

List of Acronyms

Below is the list of acronyms that have been used throughout this thesis listed in alphabetical order:

ADAS	Advanced Driver Assistance Systems
CKF	Cubature Kalman Filter
EKF	Extended Kalman Filter
KF	Kalman Filter
NIS	Normalized Innovation Squared
RMSE	Root Mean Square Error

Nomenclature

Below is the nomenclature of indices, sets, parameters, functions, and variables used throughout this thesis, listed by category.

Indices

i	Road segment index
k	Discrete time step index
m	Vehicle trail sample index
N	Total number of road segments in the road model

Sets

$\mathcal{A}_r^i$	Global arc length interval covered by road model segment i
$\mathcal{A}_{map}^i$	Global arc length interval covered by map segment i
$\boldsymbol{z}_{1:k}$	Set of all measurements available up to time step k
$\mathcal{P}_{k-1}$	Set of stored trail points at time step $k-1$

Parameters

β	Weighting factor blending road model and map based segment lengths, $\beta \in [0, 1]$
δt	Sampling interval
γ	Threshold for rejecting ambiguous lane assignments
L	Nominal clothoid segment length
M_{init}	Number of initial trail samples used for heading estimation
q_x, q_y	Longitudinal and lateral process noise variance parameters for trail point covariance inflation

ρ_{pos}	Positional consistency threshold for map data gating
ρ_{slope}	Slope consistency threshold for map data gating
w^{lane}	Lane width

Functions

$x_r(s)$	x-coordinate of the road centerline at arc length s in the local vehicle fixed frame
$y_r(s)$	y-coordinate of the road centerline at arc length s in the local vehicle fixed frame
$\kappa_r(s)$	Road curvature as a function of global arc length s
$\kappa_r^i(s)$	Curvature of segment i as a function of local arc length
$\varphi_r(s)$	Road heading as a function of global arc length s
$\varphi_r^i(s)$	Heading of segment i as a function of local arc length
$\kappa_r^{map}(s)$	Map curvature as a function of global arc length s
$\tilde{x}_r^i(s)$	Taylor-approximated x-coordinate of road segment i at arc length s
$\tilde{y}_r^i(s)$	Taylor-approximated y-coordinate of road segment i at arc length s
$\hat{x}(s_m; \boldsymbol{\theta})$	Predicted x-coordinate at arc length s_m for parameter vector $\boldsymbol{\theta}$
$\hat{y}(s_m; \boldsymbol{\theta})$	Predicted y-coordinate at arc length s_m for parameter vector $\boldsymbol{\theta}$
$\mathbf{r}_m(\boldsymbol{\theta})$	Residual vector between observed and predicted position at trail sample m
$r_{x,m}(\boldsymbol{\theta})$	Residual in the x-direction for trail sample m
$r_{y,m}(\boldsymbol{\theta})$	Residual in the y-direction for trail sample m
$\mathbf{R}(-\Delta\psi_k)$	Rotation matrix for the incremental heading change $\Delta\psi_k$

Variables

C	Cosine term evaluated at the Taylor expansion point
c^i	Curvature rate of road segment i
$c^{map,i}$	Curvature rate of map segment i
c^N	Curvature rate of the newly appended segment
δ_j	Lateral offset of the vehicle trail under lane hypothesis H_j
$\Delta\mathbf{p}_k$	Incremental ego vehicle displacement at time step k

$\Delta\psi_k$	Incremental ego vehicle heading change at time step k
Δs_i	Local arc length measured from the start of road segment i
Δs_i^{map}	Local arc length measured from the start of map segment i
$d_{x,k}$, $d_{y,k}$	Longitudinal and lateral displacement of the ego vehicle at time step k
d_k	Distance traveled by the ego vehicle between time steps k and k+1
$d_k^{e_l}$	Distance from road centerline to left road edge at time step k
$d_k^{e_r}$	Distance from road centerline to right road edge at time step k
H_j	Lane hypothesis $j \in \{0, 1, 2\}$: ego lane, left adjacent lane, right adjacent lane
j^*	Index of the selected most-likely lane hypothesis
κ_0^i	Initial curvature of road segment i
$\kappa_0^{map,i}$	Initial curvature of map segment i
ℓ^n	Length of segment n
$\ell^{road,n}$	Length of road model segment n
$\ell^{map,n}$	Length of map data segment n
ℓ^{new}	Length of a newly appended road segment
M	Number of samples in the vehicle trail
M_k	Number of stored trail points at time step k
μ_j	Predicted mean lateral position under lane hypothesis H_j
$\boldsymbol{\nu}$	Innovation vector
ν_i	Scalar residual at arc length sample s_i
$\mathbf{p}_{m,k}$	Position of the mth trail point at time step k
$\mathbf{P}_{k\|k}$	Posterior covariance of the road state at time step k
$\mathbf{P}_{k\|k-1}$	Predicted covariance of the road state at time step k
φ_0^i	Initial heading of road segment i
$\dot{\psi}_k$	Ego vehicle yaw rate at time step k
$\mathbf{Q}$	Process noise covariance matrix
$\mathbf{r}_k$	Road state vector at time step k
$\hat{\mathbf{r}}_{k\|k}$	Posterior mean of the road state at time step k
$\mathbf{R}_k$	Measurement noise covariance matrix at time step k
s	Global arc length coordinate along the road
s_m	Arc length coordinate of trail sample m
s_{start}	Global arc length at the start of a newly appended segment
s_{end}	Global arc length at the end of a newly appended segment

S	Sine term evaluated at the Taylor expansion point
$\mathbf{S}_k$	Innovation covariance matrix at time step k
$\mathbf{\Sigma}_{m,k}$	Position covariance matrix of trail point m at time step k
$\sigma^2_{x,m,k}$, $\sigma^2_{y,m,k}$	Longitudinal and lateral variance of trail point m at time step k
$\sigma_{xy,m,k}$	Cross-covariance of trail point m at time step k
σ^2_j	Predicted lateral variance under lane hypothesis H_j
$\sigma^2_{\mathrm{y},1}$	Lateral detection uncertainty variance of the first trail point
$\boldsymbol{\theta}$	Clothoid parameter vector used in vehicle trail fitting
$\hat{\boldsymbol{\theta}}$	Estimated clothoid parameter vector from weighted nonlinear least squares
v_k	Ego vehicle speed at time step k
$\mathbf{x}$	Generic parameter vector in the least-squares formulation
$x_{m,k}$, $y_{m,k}$	Cartesian coordinates of trail point m at time step k
$y^{meas}(s_i)$	Measured lateral position at arc length s_i
y^{off}_k	Lateral offset of the ego vehicle from the road centerline at time step k

Contents

List of Acronyms **ix**

Nomenclature **xi**

List of Figures **xix**

List of Tables **xxi**

1 Introduction **1**
1.1 Structure of this work 2
1.1.1 Assumptions 2
1.1.2 Limitations 2
1.2 Problem statement 3

2 Road Model **5**
2.1 The Clothoid Curve 5
2.2 Parametric Representation and Segmentation 6
2.2.1 Continuity Constraints 7
2.3 Clothoid Approximation 7
2.4 Dead Reckoning 8

3 Estimation Theory **11**
3.1 Bayesian Estimation and Filtering 11
3.1.1 The Kalman Filter 13
3.1.2 The Extended Kalman Filter 13
3.1.3 The Cubature Kalman Filter 14
3.1.4 Normalized Innovation Squared 16
3.2 Weighted Nonlinear Least Squares 16

4 Problem Formulation **19**
4.1 Formal Problem Formulation 19
4.2 Road State 19
4.3 Measurement Sources 21
4.4 Estimation Objective 21

5 Process Model **23**
5.1 State Transition 23

5.1.1 Adaptive Segment Lengths 26
5.2 Process Noise 27
5.3 Prediction Step 28

6 Vehicle Trail 31
6.1 Concept and Motivation 31
6.2 Selection Criteria for Vehicle Trail Measurements 31
6.3 Vehicle Position Propagation and Uncertainty 32
6.4 Clothoid Fitting via Weighted Nonlinear Least Squares 34
6.4.1 Measurements and Parameters 34
6.4.2 Residual Vector 35
6.4.3 Weighted Nonlinear Least Squares Objective 35
6.4.4 Initialization 35
6.5 Lane Assignment 36
6.6 Integration into the Measurement Framework 37

7 Measurement Models 39
7.1 Input Data and Sensor Overview 39
7.2 General Measurement Model 40
7.3 NIS Tuning and Gating 41
7.4 Map Data Gating 42
7.5 Update step 43

8 Results 45
8.1 Experimental Setup 45
8.1.1 Parameter Settings 46
8.2 Filter Performance Across Different Scenarios 47
8.2.1 Highway Scenario 47
8.2.2 Snow-Covered Rural Scenario 1 49
8.2.3 Snow-Covered Rural Scenario 2 50
8.2.4 Snow-Covered Rural Scenario 3 52
8.2.5 Snow-Covered Rural Scenario 4 53
8.3 Vehicle Trail Scenario 54
8.4 Dynamic Segment Lengths 55

9 Discussion 59
9.1 Overall Filter Performance 59
9.2 Performance Analysis Across Scenarios 60
9.2.1 Highway Scenario 60
9.2.2 Snow-Covered Rural Scenarios 60
9.3 Vehicle Trail Evaluation 61
9.4 Dynamic Segment Lengths 62

10 Conclusion and Future Work 65
10.1 Conclusion 65
10.2 Future Work 66

Bibliography **67**

A NIS Highway Scenario **I**

B NIS for Snow-Covered Rural Scenario 2 **VII**

List of Figures

2.1 Euler Spiral (Clothoid) 6

3.1 State space model (dynamic Bayesian network) with hidden states $\boldsymbol{x}_k$ and observed measurements $\boldsymbol{y}_k$. 12

4.1 Ego vehicle and road state parameters. 20
4.2 Ego vehicle and road segments 20
4.3 Ego vehicle with measurement sources 21

8.1 Snapshot of the tested highway scenario under good conditions. . . . 47
8.2 RMSE evaluation for the highway scenario, comparing road features only, namely lane markings, road edges, and barriers, road features combined with moving vehicles, and all measurement sources, as well as RMSE over time at selected distances using all measurement sources. 48
8.3 Measurement availability analysis for the highway scenario, showing availability over the highway scenario and over time. 48
8.4 Confusion matrix comparing the true lane class with the predicted lane class for left lane, same lane, and right lane. 49
8.5 Snow-covered rural scenario 1 with mostly clear centerline but snow covering road edges and right lane marking. 49
8.6 RMSE evaluation for snow-covered rural scenario 1. 50
8.7 Measurement availability analysis for snow-covered rural scenario 1. . 50
8.8 Snow-covered rural scenario 2 with partially faded lane markings and snow-covered road edges. 51
8.9 RMSE evaluation for the snow-covered rural scenario 2. 51
8.10 Measurement availability analysis for the snow-covered rural scenario 2. 51
8.11 Snow-covered rural scenario 3 with snow-covered lane markings and road edges. 52
8.12 RMSE evaluation for the snow-covered rural scenario 3. 52
8.13 Measurement availability analysis for the snow-covered rural scenario 3. 53
8.14 Snow-covered rural scenario 4 with partially snow-covered lane marking and road edges. 53
8.15 RMSE evaluation for the snow-covered rural scenario 4. 54
8.16 Measurement availability analysis for the snow-covered rural scenario 4. 54

8.17 Scenario for vehicle trail following. 55
8.18 RMSE evaluation using vehicle trail as the only measurement. 55
8.19 Comparison of total segment length over time using dynamic and static segment lengths. 56
8.20 Comparison of mean RMSE using dynamic and static segment lengths. 56
8.21 Mean length of last segment as a function of road curvature 57

A.1 Overview of the NIS analysis for the left lane markings. II
A.2 Overview of the NIS analysis for the right lane markings. II
A.3 Overview of the NIS analysis for the left road edges. III
A.4 Overview of the NIS analysis for the right road edges. III
A.5 Overview of the NIS analysis for the left barriers. IV
A.6 Overview of the NIS analysis for the right barriers. IV
A.7 Vehicle Trail NIS V

B.1 Overview of the NIS analysis for the left lane markings. VIII
B.2 Overview of the NIS analysis for the right lane markings. VIII
B.3 Overview of the NIS analysis for the left road edges. IX
B.4 Overview of the NIS analysis for the right road edges. IX
B.5 Overview of the NIS analysis for the left barriers. X
B.6 Overview of the NIS analysis for the right barriers. X
B.7 Overview of the NIS analysis for the vehicle trails. XI

List of Tables

8.1 Process noise standard deviations used to construct the covariance matrix Q. . . . 46
8.2 Initialization of the state estimate $\hat{\boldsymbol{r}}_{0|0}$. . . . 46
8.3 Initial standard deviations used to construct the covariance matrix $P_{0|0}$. 46
8.4 Lateral measurement noise standard deviation models used for the different measurement sources. . . . 47

1 Introduction

Advanced Driver Assistance Systems (ADAS) play a central role in the modern automotive industry by helping drivers maintain safe and stable vehicle operation. These systems rely on a combination of cameras, radar, and other onboard sensors to perceive the surrounding environment, detect relevant objects, and support driving decisions [1], [2]. A key capability within ADAS is road estimation, which refers to the process of interpreting the road environment and estimating its geometry, boundaries, lane structure, and the vehicle's position relative to the drivable path. This information is essential for functions such as lane keeping assistance, lane departure warning, adaptive cruise control, and trajectory planning.

Achieving robust road estimation is challenging due to the variability of real world driving environments. Adverse weather, poor illumination, worn or missing lane markings, and complex traffic situations can significantly reduce the reliability of vision based approaches [3]. Although cameras provide rich and high resolution visual information, their sensitivity to lighting and weather conditions limits their robustness in challenging scenarios.

To address these limitations and improve robustness, modern ADAS increasingly incorporate additional sensing modalities into the road estimation pipeline. Radar provides complementary information that is less affected by illumination changes and can improve the robustness of road estimation under adverse weather conditions [4]. In addition to onboard sensor data, map information can provide prior knowledge about the road structure, thereby supporting road estimation even when local sensor observations are uncertain or incomplete [5], [6].

Surrounding vehicles can also serve as an important source of information about the road layout [7], [8]. The trajectories and positions of other vehicles can be used to describe road geometry and drivable space, particularly in situations where lane markings or road boundaries are partially unclear or degraded [7], [8]. By combining sensor measurements, map data, and information from surrounding vehicles through multi-modal sensor fusion, ADAS can achieve a more robust and reliable estimation of the road environment.

1.1 Structure of this work

The thesis begins by introducing the mathematical road representation and clothoid based modeling approach in Chapter 2. Chapter 3 reviews the estimation techniques relevant to this work, including Bayesian filtering, Extended Kalman Filtering, Cubature Kalman Filtering, and nonlinear least squares methods. The proposed estimation framework is formulated in Chapter 4 and further developed through the process and measurement models in Chapters 5 and 7, respectively. Chapter 6 presents the vehicle trail formulation and clothoid fitting procedure. The performance and the results of the proposed framework is evaluated experimentally in Chapter 8, followed by a discussion in Chapter 9 and concluding remarks in Chapter 10.

1.1.1 Assumptions

To limit the scope of the problem, the road estimation framework is assumed to represent the road ahead using multiple connected segments that together describe the current road. More complex road structures, such as intersections, exits, and forks, are not explicitly modeled. The estimation problem is therefore restricted to the road currently followed by the ego vehicle.

The road geometry is further assumed to be representable in a flat two-dimensional plane. Consequently, slope, elevation changes, and other vertical road profile effects are not included in the model. This assumption is motivated by the available observations and the chosen problem formulation, but it may reduce estimation accuracy in environments with significant height variations.

1.1.2 Limitations

Roads can take many different forms, and their characteristics may vary significantly depending on the environment, design standards, traffic conditions, and operational context. Because of this diversity, there are numerous scenarios and special cases that may influence how a road should be analyzed or evaluated.

One limitation of this thesis is that it will focus only on a specific set of conditions rather than attempting to address every possible road type or situation. This approach allows for a more detailed and contextual understanding of the selected conditions, while acknowledging that the findings may not be universally applicable to all road environments.

Another limitation is that the framework is evaluated against a reference centerline reconstructed from onboard sensor data rather than true ground truth. This reference is obtained by integrating the ego vehicle speed and heading over time and estimating the lateral centerline position as the mean of the observed left and right lane marking offsets. As a result, the reference itself is subject to the same sensor degradation and measurement noise that affect the filter under evaluation, particularly in the snow-covered rural scenarios where lane marking availability is low. This means that the reported RMSE values should be interpreted as a measure of consistency between the filter estimate and the reconstructed reference, rather than as absolute estimation error with respect to the true road geometry.

1.2 Problem statement

This project addresses the problem of improving road estimation within ADAS by investigating how multiple sources of information can be used to better describe the road geometry. In particular, the work focuses on combining information from onboard perception systems, map data, and surrounding vehicles in order to improve robustness under challenging conditions. The objective is to develop and evaluate an approach that can provide accurate and consistent estimates of road geometry across a wide range of environments.

2

Road Model

The road geometry ahead of the ego vehicle must be represented in a compact and accurate form that is suitable for recursive estimation. Many representations exist, including polynomials and circular arcs, but these become inaccurate at longer ranges [9]. In this work the road is modeled as a clothoid, also known as an Euler spiral, which provides a more accurate description of road geometry at longer ranges, and is consistent with how roads are designed in practice. This chapter introduces the clothoid model, describes how the road is represented as a sequence of connected clothoid segments, derives the Taylor series approximation used to evaluate the clothoid integrals, and introduces dead reckoning.

2.1 The Clothoid Curve

A clothoid is a planar curve whose curvature varies linearly with arc length. This property makes it particularly well suited for modeling road geometry, as it captures the gradual curvature changes found in real roads and is the curve type used in road design standards for transition curves between straight segments and circular arcs [10], [11], [12].

The parametric form of a clothoid is expressed using Fresnel integrals [11]:

$$X(j) = a \int_0^j \cos\left(\frac{\pi}{2} u^2\right) du, \tag{2.1}$$

$$Y(j) = a \int_0^j \sin\left(\frac{\pi}{2} u^2\right) du, \tag{2.2}$$

where $X(t)$ and $Y(t)$ are the curve coordinates, j is a path parameter related to the arc length, and a is a scaling factor controlling the rate of curvature change. The curvature at parameter j is

$$\kappa(j) = \frac{\pi j}{a}, \tag{2.3}$$

and the tangent angle is

$$\phi(j) = \frac{\pi}{2} j^2. \tag{2.4}$$

A key property of the clothoid is that it satisfies G^2 continuity conditions, meaning

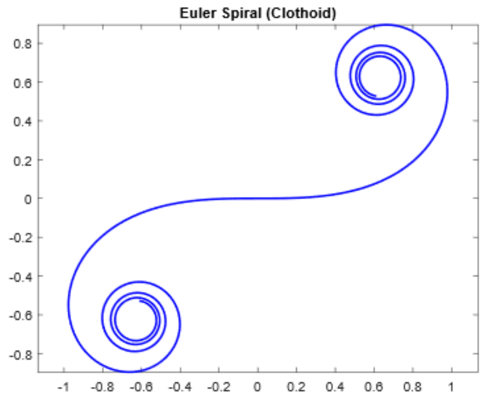

Figure 2.1: Euler Spiral (Clothoid)

that position, heading, and curvature are all continuous along the curve. This ensures smooth transitions between road segments and is a requirement for physically realistic road models [13].

2.2 Parametric Representation and Segmentation

Following [9], the road ahead of the ego vehicle is represented as a sequence of N connected clothoid segments, indexed by $i = 1, \dots, N$. Each segment i is parameterised by a local arc length $s \in [0, L]$, where L denotes the segment length. The curvature of segment i varies linearly with arc length as

$$\kappa^i(s) = \kappa_0^i + c^i s, \tag{2.5}$$

where κ_0^i is the initial curvature of segment i and $c^i = \frac{d\kappa^i}{ds}$ is the curvature rate of segment i. The heading along segment i is obtained by integrating the curvature:

$$\varphi^i(s) = \varphi_0^i + \kappa_0^i s + \frac{c^i}{2} s^2, \tag{2.6}$$

and the curve coordinates are

$$\begin{bmatrix} x^i(s) \\ y^i(s) \end{bmatrix} = \begin{bmatrix} x_0^i \\ y_0^i \end{bmatrix} + \int_0^s \begin{bmatrix} \cos\left(\varphi^i(t)\right) \\ \sin\left(\varphi^i(t)\right) \end{bmatrix} dt. \tag{2.7}$$

where φ_0^i is the initial heading of segment i and (x_0^i, y_0^i) are the starting coordinates of segment i. The segments are fixed to the road, and their lengths are updated as the ego vehicle travels forward. When the ego vehicle passes the end of the nearest segment, that segment along with its curvature rate c^i is discarded and a new segment is appended at the far end of the road representation. This rolling structure ensures that the road model always covers the relevant range ahead of the ego vehicle.

2.2.1 Continuity Constraints

To ensure a physically smooth road representation, G^2 continuity is enforced at the junction between consecutive segments [14]. This requires that position, heading, and curvature match at the connection point $s = L$. For segment i, the initial conditions are determined by the end state of segment $i-1$:

$$\kappa^i = \kappa_0^{i-1} + c^{i-1}L, \tag{2.8}$$

$$\varphi_0^i = \varphi_0^{i-1} + \kappa_0^{i-1}L + \frac{c^{i-1}}{2}L^2, \tag{2.9}$$

$$\begin{bmatrix} x_0^i \\ y_0^i \end{bmatrix} = \begin{bmatrix} x^{i-1}(L) \\ y^{i-1}(L) \end{bmatrix}. \tag{2.10}$$

These constraints mean that only the curvature rate c^i of each segment is a free parameter, all other segment quantities follow from the G^2 conditions and the state of the first segment.

2.3 Clothoid Approximation

The integrals in (2.7) have no closed-form solution. To make evaluation manageable, and to allow Jacobians to be derived analytically in the process model and the vehicle trail, the cosine and sine terms are approximated using a Taylor series expansion around $\frac{L}{2}$. As noted in [9], a third-order Taylor series expansion provides sufficient accuracy for road shapes encountered in road estimation while being computationally less complex than alternative methods. Consequently, the limiting factor is the validity of the constant curvature change rate assumption over the considered segment, rather than the approximation itself. The third-order Taylor series expansion around $\frac{L}{2}$ can be derived as follows:

$$\begin{aligned} \tilde{x}_r^i(s) = x_0^i &+ \left(\frac{S\dot{\alpha}^3}{24} - \frac{cC\dot{\alpha}}{8}\right)s^4 \\ &+ \left(-\frac{L\left(\frac{S\dot{\alpha}^3}{6} - \frac{cC\dot{\alpha}}{2}\right)}{2} - \frac{C\dot{\alpha}^2}{6} - \frac{cS}{6}\right)s^3 \\ &+ \left(\frac{L\frac{C\dot{\alpha}^2+cS}{2}}{2} - \frac{S\dot{\alpha}}{2} + \frac{3L^2\left(\frac{S\dot{\alpha}^3}{6} - \frac{cC\dot{\alpha}}{2}\right)}{8}\right)s^2 \\ &+ \left(C - \frac{L^3\left(\frac{S\dot{\alpha}^3}{6} - \frac{cC\dot{\alpha}}{2}\right)}{8} - \frac{L^2\frac{C\dot{\alpha}^2+cS}{2}}{4} + \frac{LS\dot{\alpha}}{2}\right)s \end{aligned} \tag{2.11}$$

$$
\begin{aligned}
\tilde{y}_r^i(s) = y_0^i &+ \left(-\frac{C\dot{\alpha}^3}{24} - \frac{cS\dot{\alpha}}{8}\right)s^4 \\
&+ \left(\frac{L\left(\frac{C\dot{\alpha}^3}{6} + \frac{cS\dot{\alpha}}{2}\right)}{2} - \frac{S\dot{\alpha}^2}{6} + \frac{cC}{6}\right)s^3 \\
&+ \left(\frac{C\dot{\alpha}^2}{2} + \frac{L\frac{S\dot{\alpha}^2 - cC}{2}}{2} - \frac{3L^2\left(\frac{C\dot{\alpha}^3}{6} + \frac{cS\dot{\alpha}}{2}\right)}{8}\right)s^2 \\
&+ \left(S + \frac{L^3\left(\frac{C\dot{\alpha}^3}{6} + \frac{cS\dot{\alpha}}{2}\right)}{8} + \frac{L^2\frac{S\dot{\alpha}^2 - cC}{2}}{4} - \frac{LC\dot{\alpha}}{2}\right)s
\end{aligned}
\tag{2.12}
$$

where

$$S = \sin\left(\varphi_0^i + \kappa_0^i\frac{L}{2} + c^i\frac{L^2}{8}\right), \tag{2.13}$$

$$C = \cos\left(\varphi_0^i + \kappa_0^i\frac{L}{2} + c^i\frac{L^2}{8}\right), \tag{2.14}$$

$$\dot{\alpha} = \kappa_0^i + c^i\frac{L}{2}. \tag{2.15}$$

2.4 Dead Reckoning

Dead reckoning is a navigation technique in which the current vehicle state is estimated by propagating a previously known state using onboard motion measurements [15]. Rather than relying on continuous external position updates, the method uses internally measured vehicle motion to determine how the vehicle pose evolves over time. For ground vehicles, this propagation is commonly based on wheel-speed measurements, steering angle, yaw rate, and inertial sensor data [15]. The method is widely used because it provides continuous localization and can remain available even when external infrastructure such as GNSS is temporarily unavailable or degraded [15].

For planar vehicle motion, dead reckoning updates the vehicle heading by integrating the yaw rate and updates the position by integrating the forward velocity in the heading direction. A simple discrete-time formulation is obtained by defining the vehicle state at time step k as

$$\mathbf{x}_k = \begin{bmatrix} x_k & y_k & \psi_k \end{bmatrix}^T$$

and propagated according to

$$\psi_{k+1} = \psi_k + \dot{\psi}_k \delta t$$

$$x_{k+1} = x_k + v_k \cos(\psi_k)\delta t$$

$$y_{k+1} = y_k + v_k \sin(\psi_k)\delta t$$

where v_k is the forward velocity, ψ is the vehicle yaw angle, that is, the heading of the vehicle in the global plane, $\dot{\psi}_k$ is the yaw rate, and δt is the sampling time [16]. These equations express the basic principle of dead reckoning. The heading is updated from the measured rotational motion, while the position is updated by integrating the vehicle velocity in the direction of travel.

A fundamental limitation of dead reckoning is that errors accumulate over time due to sensor noise, bias, wheel slip, and modeling inaccuracies [15]. As a result, even small measurement errors can lead to increasing deviations in the estimated position and heading, causing the estimated trajectory to gradually drift from the true vehicle motion. This effect becomes particularly significant when no absolute position updates are available for longer periods. For this reason, dead reckoning is commonly combined with other localization methods, such as GNSS or map-based corrections, in practical navigation systems [15].

3

Estimation Theory

3.1 Bayesian Estimation and Filtering

Many problems in signal processing and control theory involve estimating unknown quantities from noisy observations. Estimating unknown quantities from noisy measurements can be formulated as a probabilistic inference problem, where uncertainty in the system and the measurements is described using probability distributions. Bayesian estimation provides a principled framework for such inference. In the Bayesian framework, unknown quantities such as system states or parameters are modeled as random variables described by probability distributions. Prior knowledge about the unknown variables is represented by a prior probability distribution. When measurements become available, this prior information is updated using Bayes' theorem to obtain the posterior distribution conditioned on the observations [17]. Throughout this report, a discrete-time formulation indexed by k is used, since measurements are available at discrete sampling instants and the Bayesian filters considered here operate recursively in time.

Bayes' rule is given by

$$p(\boldsymbol{x}_k|\boldsymbol{y}_{1:k}) = \frac{p(\boldsymbol{y}_k|\boldsymbol{x}_k, \boldsymbol{y}_{1:k-1})p(\boldsymbol{x}_k|\boldsymbol{y}_{1:k-1})}{p(\boldsymbol{y}_k|\boldsymbol{y}_{1:k-1})} \tag{3.1}$$

where $p(\boldsymbol{x}_k|\boldsymbol{y}_{1:k-1})$ is the prior distribution, $p(\boldsymbol{y}_k|\boldsymbol{x}_k, \boldsymbol{y}_{1:k-1})$ the likelihood of the observations given the state, $p(\boldsymbol{y}_k|\boldsymbol{y}_{1:k-1})$ the marginal distribution and $p(\boldsymbol{x}_k|\boldsymbol{y}_{1:k})$ the posterior distribution. The general purpose of Bayesian filtering is to recursively estimate the posterior distribution by computing the marginal posterior of the state at time k, given the measurement history up to time k. Meaning, the posterior distribution summarizes all the information that the observation sequence provides about the unknown state. The objective is therefore to estimate the states of a dynamical system using the available measurements [17].

In optimal filtering, the task can be viewed as a statistical inverse problem. Meaning, given the observed noisy measurements $\{\boldsymbol{y}_k\}$, the goal is to estimate the hidden states $\{\boldsymbol{x}_k\}$ by combining a model for how the state evolves over time (process

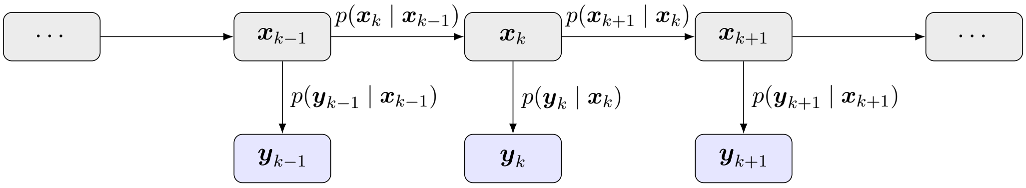

Figure 3.1: State space model (dynamic Bayesian network) with hidden states $\boldsymbol{x}_k$ and observed measurements $\boldsymbol{y}_k$.

model) with a model for how the measurements are produced (measurement model). To relate this to the Bayesian sense, the goal is to compute the joint posterior distribution for all the states given all the measurements [17]. Figure 3.1 illustrates the corresponding state space model, where the Markov transition density $p(\boldsymbol{x}_k \mid \boldsymbol{x}_{k-1})$ describes the system dynamics and the likelihood $p(\boldsymbol{y}_k \mid \boldsymbol{x}_k)$ relates each measurement to the current state.

The recursive part of a Bayesian filter consists of two main steps: a prediction step and an update step. Before using the filter equations, the initial state $\boldsymbol{x}_0$ must be initialized by specifying an initial distribution $p(\boldsymbol{x}_0)$.

- Prediction step. The predictive distribution of the state $\boldsymbol{x}_k$ can be computed by the Chapman Kolmogorov equation at time k, given the dynamic model.

$$p(\boldsymbol{x}_k \mid \boldsymbol{y}_{1:k-1}) = \int p(\boldsymbol{x}_k \mid \boldsymbol{x}_{k-1})\, p(\boldsymbol{x}_{k-1} \mid \boldsymbol{y}_{1:k-1})\, d\boldsymbol{x}_{k-1}. \tag{3.2}$$

- Update step. The posterior distribution of the state $\boldsymbol{x}_k$, given the measurement at time step k, can be computed using Bayes' Rule (3.1).

$$p(\boldsymbol{x}_k \mid \boldsymbol{y}_{1:k}) = \frac{1}{Z_k}\, p(\boldsymbol{y}_k \mid \boldsymbol{x}_k)\, p(\boldsymbol{x}_k \mid \boldsymbol{y}_{1:k-1}), \tag{3.3}$$

  where Z_k is the normalization constant given as

$$Z_k = \int p(\boldsymbol{y}_k \mid \boldsymbol{x}_k)\, p(\boldsymbol{x}_k \mid \boldsymbol{y}_{1:k-1})\, d\boldsymbol{x}_k. \tag{3.4}$$

  Note that the update step in Bayesian filtering is essentially Bayes' rule applied at time k, the denominator Z_k does not depend on $\boldsymbol{x}_k$ so the update equation can therefore be expressed as

$$p(\boldsymbol{x}_k \mid \boldsymbol{y}_{1:k}) \propto p(\boldsymbol{y}_k | \boldsymbol{x}_k, \boldsymbol{y}_{1:k-1}) p(\boldsymbol{x}_k | \boldsymbol{y}_{1:k-1}) \tag{3.5}$$

  where the posterior distribution is described as proportional to the prior and the likelihood distribution [18]. Since the noise of the measurements, in this work, is independent over time the likelihood expression can be simplified as

$$p(\boldsymbol{x}_k \mid \boldsymbol{y}_{1:k}) \propto p(\boldsymbol{y}_k | \boldsymbol{x}_k) p(\boldsymbol{x}_k | \boldsymbol{y}_{1:k-1}) \tag{3.6}$$

Note that the prior in Bayesian filtering is the predicted distribution $p(\boldsymbol{x}_k \mid \boldsymbol{y}_{1:k-1})$ obtained from the previous posterior.

3.1.1 The Kalman Filter

When the system dynamics and measurement models are linear and the process and measurement noises are Gaussian, the Kalman filter works as the closed form solution to the Bayesian filtering equations. A discrete-time linear Gaussian state space model can be expressed as

$$\begin{aligned} \boldsymbol{x}_k &= A_{k-1}\boldsymbol{x}_{k-1} + \boldsymbol{q}_{k-1}, && (3.7) \\ \boldsymbol{y}_k &= H_k\boldsymbol{x}_k + \boldsymbol{r}_k. && (3.8) \end{aligned}$$

where $\boldsymbol{q}_{k-1} \sim \mathcal{N}(0, Q_{k-1})$ is the process noise and $\boldsymbol{r}_k \sim \mathcal{N}(0, R_k)$ is the measurement noise. Let $\boldsymbol{x}_k \in \mathbb{R}^n$ denote the state vector and $\boldsymbol{y}_k \in \mathbb{R}^m$ the measurement vector, where n and m are their respective dimensions [17] . The Kalman filter then, as mention in the previous section, calculates the posterior density through a prediction and update step. The Kalman filter equations are given by

- Prediction step.

$$\begin{aligned} \hat{\boldsymbol{x}}_{k|k-1} &= A_{k-1}\hat{\boldsymbol{x}}_{k-1|k-1}, && (3.9) \\ P_{k|k-1} &= A_{k-1}P_{k-1|k-1}A_{k-1}^{\top} + Q_{k-1}. && (3.10) \end{aligned}$$

  where $\hat{\boldsymbol{x}}_{k|k-1}$ and $P_{k|k-1}$ are the predicted state estimate and covariance, A_{k-1} is the state transition matrix, and Q_{k-1} is the process noise covariance. [17].

- Update step.

$$\begin{aligned} \boldsymbol{v}_k &= \boldsymbol{y}_k - H_k\hat{\boldsymbol{x}}_{k|k-1}, && (3.11) \\ S_k &= H_kP_{k|k-1}H_k^{\top} + R_k, && (3.12) \\ K_k &= P_{k|k-1}H_k^{\top}S_k^{-1}, && (3.13) \\ \hat{\boldsymbol{x}}_{k|k} &= \hat{\boldsymbol{x}}_{k|k-1} + K_k\boldsymbol{v}_k, && (3.14) \\ P_{k|k} &= P_{k|k-1} - K_kS_kK_k^{\top}. && (3.15) \end{aligned}$$

where H_k is the (linear) measurement matrix, $\boldsymbol{v}_k$ is the innovation (measurement residual), S_k is the innovation covariance, K_k is the Kalman gain, R_k is the measurement noise covariance, and $\hat{\boldsymbol{x}}_{k|k}$ and $P_{k|k}$ are the posterior (updated) state mean and covariance, respectively. Together with $\boldsymbol{x}_0$, the initial error covariance P_0 must be specified before implementing the filter [17].

3.1.2 The Extended Kalman Filter

In many real systems, the motion model and the sensor model are not linear, so the standard Kalman filter cannot be used as it is. However, the filtering distribution can in many cases still be approximated with a Gaussian. One method which can be used for such implementation is the extended Kalman filter [19]. In contrast to the standard Kalman filter the equations for the extended Kalman filter can be given by

$$\boldsymbol{x}_k = f(\boldsymbol{x}_{k-1}) + \boldsymbol{q}_{k-1}, \tag{3.16}$$

$$\boldsymbol{y}_k = h(\boldsymbol{x}_k) + \boldsymbol{r}_k, \tag{3.17}$$

where the notation is the same as for the linear Kalman filter, except that $f(\cdot)$ denotes the dynamic model and $h(\cdot)$ denotes the measurement model. The main idea of the extended Kalman filter is to approximate the filtering distributions by Gaussian approximations. This is achieved by linearizing the nonlinear functions using a first-order Taylor series expansion around the current state estimate [19]. The EKF follows the same prediction and update structure as the standard KF, with the equations given by

- Prediction step.

$$\hat{\boldsymbol{x}}_{k|k-1} = f\left(\hat{\boldsymbol{x}}_{k-1|k-1}\right), \tag{3.18}$$

$$F_{k-1} = \left.\frac{\partial f(\boldsymbol{x})}{\partial \boldsymbol{x}}\right|_{\boldsymbol{x}=\hat{\boldsymbol{x}}_{k-1|k-1}}, \tag{3.19}$$

$$P_{k|k-1} = F_{k-1} P_{k-1|k-1} F_{k-1}^{\top} + Q_{k-1}. \tag{3.20}$$

- Update step.

$$\boldsymbol{v}_k = \boldsymbol{y}_k - h\left(\hat{\boldsymbol{x}}_{k|k-1}\right), \tag{3.21}$$

$$H_k = \left.\frac{\partial h(\boldsymbol{x})}{\partial \boldsymbol{x}}\right|_{\boldsymbol{x}=\hat{\boldsymbol{x}}_{k|k-1}}, \tag{3.22}$$

$$S_k = H_k(\hat{\boldsymbol{x}}_{k|k-1}) P_{k|k-1} H_k^{\top}(\hat{\boldsymbol{x}}_{k|k-1}) + R_k, \tag{3.23}$$

$$K_k = P_{k|k-1} H_k^{\top}(\hat{\boldsymbol{x}}_{k|k-1}) S_k^{-1}, \tag{3.24}$$

$$\hat{\boldsymbol{x}}_{k|k} = \hat{\boldsymbol{x}}_{k|k-1} + K_k \boldsymbol{v}_k, \tag{3.25}$$

$$P_{k|k} = P_{k|k-1} - K_k S_k K_k^{\top}. \tag{3.26}$$

where F_{k-1} and H_k denote the Jacobian matrices of the functions $f(\cdot)$ and $h(\cdot)$, respectively. The Jacobians are used to obtain a local linear approximation of the nonlinear models around $\hat{\boldsymbol{x}}_{k|k-1}$, via a first-order Taylor expansion. This is a common filtering choice due to its simplicity in relation to its performance. A disadvantage of the EKF is that the same simplification, the use of a local linear approximation, can make it unreliable when used in problems with considerable non-linearities [19].

3.1.3 The Cubature Kalman Filter

To handle nonlinear models without using linearization or computing Jacobians, the cubature Kalman filter (CKF) is a commonly used method. The CKF approximates the Gaussian integrals in the prediction and update steps by evaluating the nonlinear functions at a set of cubature points and combining the results with fixed weights [20]. Consider the nonlinear state-space model in (3.16). The corresponding CKF prediction and update equations are given by

- Prediction step

$$\boldsymbol{\xi}_i = \begin{cases} \sqrt{n}\,\boldsymbol{e}_i & i = 1, \ldots, n, \\ -\sqrt{n}\,\boldsymbol{e}_{i-n} & i = n+1, \ldots, 2n, \end{cases} \tag{3.27}$$

$$W_i = \frac{1}{2n}, \tag{3.28}$$

$$\boldsymbol{\chi}_{k-1}^{(i)} = \hat{\boldsymbol{x}}_{k-1|k-1} + \sqrt{P_{k-1|k-1}}\,\boldsymbol{\xi}_i, \tag{3.29}$$

$$\hat{\boldsymbol{\chi}}_{k|k-1}^{(i)} = f(\boldsymbol{\chi}_{k-1}^{(i)}), \tag{3.30}$$

$$\hat{\boldsymbol{x}}_{k|k-1} = \sum_{i=1}^{2n} W_i \hat{\boldsymbol{\chi}}_{k|k-1}^{(i)}, \tag{3.31}$$

$$P_{k|k-1} = \sum_{i=1}^{2n} W_i \left(\hat{\boldsymbol{\chi}}_{k|k-1}^{(i)} - \hat{\boldsymbol{x}}_{k|k-1}\right)\left(\hat{\boldsymbol{\chi}}_{k|k-1}^{(i)} - \hat{\boldsymbol{x}}_{k|k-1}\right)^\top + Q_k. \tag{3.32}$$

  where $\boldsymbol{\xi}_i$ are the $2n$ cubature points with weight $W_i = \frac{1}{2n}$, $\boldsymbol{e}_i$ denotes a unit vector in the direction of the coordinate axis i and $\boldsymbol{\chi}_{k-1}^{(i)}$ and $\hat{\boldsymbol{\chi}}_{k|k-1}^{(i)}$ denote the cubature points before and after propagation through $f(\cdot)$ [19].

- Update step.

$$\boldsymbol{\chi}_{k|k-1}^{(i)} = \hat{\boldsymbol{x}}_{k|k-1} + \sqrt{P_{k|k-1}}\,\boldsymbol{\xi}_i, \tag{3.33}$$

$$\hat{\boldsymbol{z}}_{k|k-1}^{(i)} = h\Big(\boldsymbol{\chi}_{k|k-1}^{(i)}\Big), \tag{3.34}$$

$$\hat{\boldsymbol{z}}_k = \sum_{i=1}^{2n} W_i \hat{\boldsymbol{z}}_{k|k-1}^{(i)}, \tag{3.35}$$

$$S_k = \sum_{i=1}^{2n} W_i \left(\hat{\boldsymbol{z}}_{k|k-1}^{(i)} - \hat{\boldsymbol{z}}_k\right)\left(\hat{\boldsymbol{z}}_{k|k-1}^{(i)} - \hat{\boldsymbol{z}}_k\right)^\top + R_k, \tag{3.36}$$

$$C_k = \sum_{i=1}^{2n} W_i \left(\boldsymbol{\chi}_{k|k-1}^{(i)} - \hat{\boldsymbol{x}}_{k|k-1}\right)\left(\hat{\boldsymbol{z}}_{k|k-1}^{(i)} - \hat{\boldsymbol{z}}_k\right)^\top, \tag{3.37}$$

$$K_k = C_k S_k^{-1}, \tag{3.38}$$

$$\hat{\boldsymbol{x}}_{k|k} = \hat{\boldsymbol{x}}_{k|k-1} + K_k\left(\boldsymbol{z}_k - \hat{\boldsymbol{z}}_k\right), \tag{3.39}$$

$$P_{k|k} = P_{k|k-1} - K_k S_k K_k^\top. \tag{3.40}$$

where $\hat{\boldsymbol{z}}_{k|k-1}^{(i)}$ are the predicted measurement cubature points obtained by propagating $\boldsymbol{\chi}_{k|k-1}^{(i)}$ through the measurement function $h(\cdot)$, $\hat{\boldsymbol{z}}_k$ is the predicted measurement mean and C_k is cross covariance of the state and the measurement [19].

3.1.4 Normalized Innovation Squared

In Bayesian estimation, incorrect or inconsistent measurements can worsen the state estimate and may, in some cases, even lead to filter divergence. In the context of road geometry estimation, this can occur due to surrounding vehicles performing lane changes, lane split scenarios or highway exits. To address this issue, validation gating is commonly applied before the measurement update step. A widely used approach is the Normalized Innovation Squared (NIS) gating method, which evaluates the statistical consistency between the predicted measurement and the received observation (measurement) [21]. The innovation, also often referred to as the residual, is defined as the difference between the actual measurement and the predicted measurement obtained from the current state estimate. Since the innovation is influenced by both measurement uncertainty and state uncertainty, its value from the innovation alone is not sufficient to determine whether a measurement is valid or not. Instead, the innovation is normalized using the innovation covariance matrix, resulting in the following NIS statistic

$$\epsilon_\nu = \nu^T S^{-1} \nu \tag{3.41}$$

where ν denotes the innovation vector and S represents the innovation covariance matrix. Under the assumption of Gaussian noise, the NIS follows a chi-square distribution with degrees of freedom corresponding to the measurement dimension [21]. Based on this criterion, a measurement is only accepted if the computed NIS value lies below a predefined chi-square threshold. This process is commonly referred to as validation gating or statistical gating. Measurements outside the validation gate are rejected because they are considered statistically inconsistent with the predicted state [21].

3.2 Weighted Nonlinear Least Squares

In least-squares problems, the objective function has a special structure that can be leveraged to develop efficient optimization algorithms [22]. The objective is defined as the sum of squared residuals,

$$f(\boldsymbol{x}) = \frac{1}{2} \sum_{j=1}^{m} r_j^2(\boldsymbol{x}), \tag{3.42}$$

where each $r_j : \mathbb{R}^n \to \mathbb{R}$ is a smooth residual function, and typically $m \geq n$. Here, j indexes the residuals, m denotes the number of residuals, and n denotes the number of unknown parameters in the generic least-squares problem. This notation is local to this section and is independent of the segment indexing used elsewhere in the thesis. By minimizing f, the parameter vector $\boldsymbol{x}$ is chosen such that the model best fits the observed data.

When the observations are corrupted by independent Gaussian noise with variances σ_j^2, the maximum likelihood estimation is equivalent to a weighted nonlinear least squares problem [23]. Each residual is scaled by its standard deviation, giving more weight to reliable observations and less weight to uncertain ones:

$$f(\boldsymbol{x}) = \frac{1}{2} \sum_{j=1}^{m} \frac{r_j^2(\boldsymbol{x})}{\sigma_j^2}. \tag{3.43}$$

Minimizing this objective is equivalent to maximizing the likelihood of the observations given the parameters under the Gaussian noise assumption.

Since the residuals $r_j(\boldsymbol{x})$ are nonlinear in $\boldsymbol{x}$, the problem has no closed form solution and must be solved iteratively. The Levenberg-Marquardt algorithm is used, which at each iteration computes the update

$$\Delta \boldsymbol{x}^j = -\left(J^T J + \lambda I\right)^{-1} J^T \boldsymbol{r}(\boldsymbol{x}^j), \tag{3.44}$$

where J is the Jacobian of the residual vector with respect to $\boldsymbol{x}$, evaluated at the current estimate $\boldsymbol{x}^j$, and $\lambda \geq 0$ is a damping parameter adjusted automatically at each iteration. When λ is large the step resembles gradient descent, providing stability far from the solution. When λ is small the step approaches the Gauss-Newton solution, providing fast convergence near the solution [22].

Since the problem is nonlinear, convergence to the global minimum is not guaranteed and the solution may depend on the initial parameter guess $\boldsymbol{x}^0$. A good initialization is therefore important to ensure the optimizer converges to a physically meaningful solution, as discussed further in Section 6.4.4.

4

Problem Formulation

4.1 Formal Problem Formulation

Building on the motivation in Section 1.2, the estimation problem is now stated precisely. The goal of this work is to estimate the road geometry ahead of the ego vehicle by fusing measurements from multiple onboard sensors and map data within a Kalman filter framework. Specifically, the aim is to estimate the road centerline position, heading, and curvature at both short and long ranges, represented by the state vector defined in Section 4.2.

Two specific research questions are investigated. First, whether incorporating map data and moving vehicle observations as additional measurement sources improves the road geometry estimate compared to using road features (lane markings, road edges, and barriers) alone. This is particularly relevant at longer ranges where road features become unreliable, and in situations where surrounding vehicles provide implicit information about the road geometry ahead. Second, how robust is the filter under challenging driving conditions, particularly snow-covered roads, where sensor based measurements may be partially or fully unavailable due to degraded detection quality, ambiguous observations, or faulty detections?

4.2 Road State

The road geometry is described by a state vector $\mathbf{r}_k$ at discrete time k, defined following [9] and extended here to include the distances to the left and right road edges:

$$\mathbf{r}_k = \begin{bmatrix} y_k^{\text{off}} & \varphi_k & \kappa_{0,k} & c_k^1 & \cdots & c_k^N & w_k^{\text{lane}} & d_k^{e_r} & d_k^{e_l} \end{bmatrix}^\top, \tag{4.1}$$

where y_k^{off} is the lateral offset of the ego vehicle from the road centerline, φ_k is the current road heading relative to the ego vehicle, $\kappa_{0,k}$ is the initial curvature of the first clothoid segment, $c_k^1, \ldots, c_k^N$ are the curvature rates of the N road segments, w_k^{lane} is the lane width, and $d_k^{e_r}$ and $d_k^{e_l}$ are the distances from the road centerline to the right and left road edges, respectively. The clothoid segmentation and the role of each parameter are described in detail in Chapter 2.

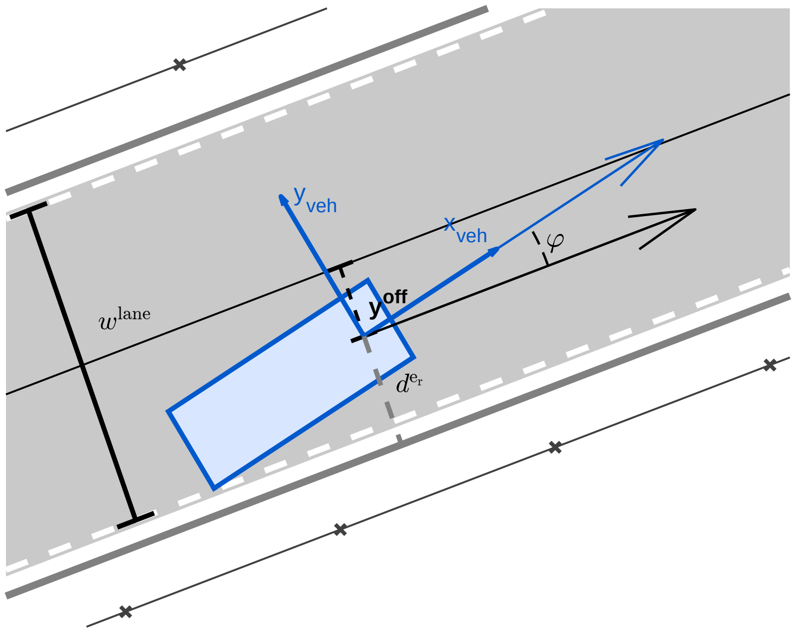

Figure 4.1: Ego vehicle and road state parameters.

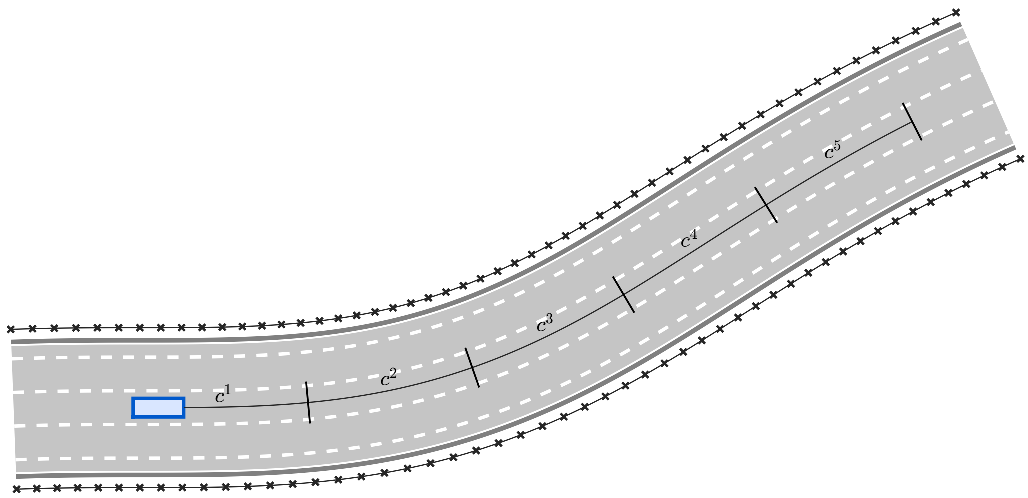

Figure 4.2: Ego vehicle and road segments

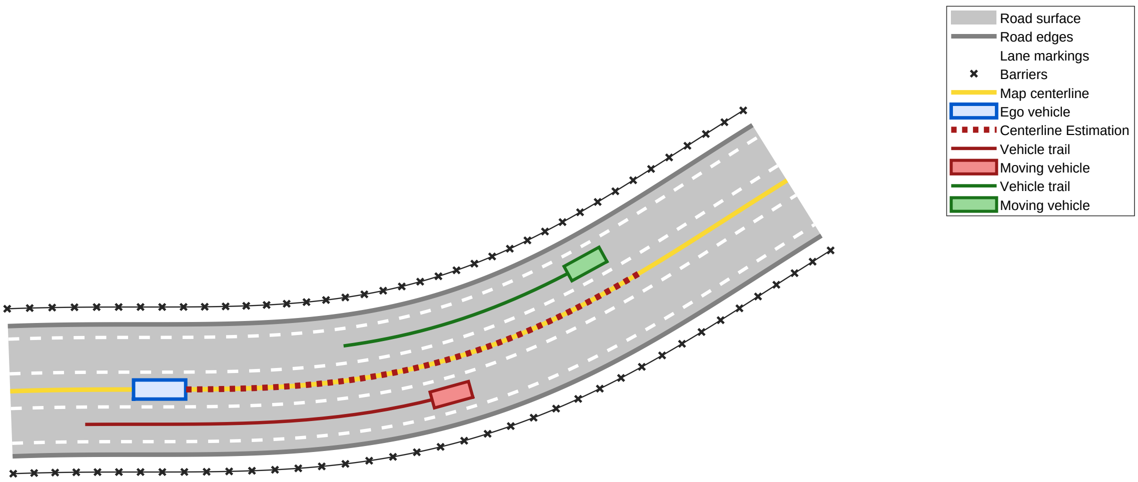

Figure 4.3: Ego vehicle with measurement sources

4.3 Measurement Sources

The road state is estimated by fusing measurements from multiple onboard sensors and map data. Some measurements include a confidence indicator reflecting their reliability, which is used to weight their contribution to the filter.

Lane markings, road edges, and road barriers are detected by the onboard sensors and provided as clothoid parametrization in the ego vehicle coordinate frame, starting at the ego vehicle position. Each is described by a lateral offset, heading angle, curvature, and curvature rate. These measurements also come with a maximum valid range, beyond which the measurement is considered unreliable.

In this work, map data is assumed to provide a prebuilt description of the road ahead, represented using the same segmented clothoid structure as the road model, with each segment characterized by its length, curvature and curvature rate. Unlike the other measurements, map data does not provide a lateral offset and therefore does not directly constrain y^{off}. It does however contribute information about the road shape through the heading, curvature, and curvature rate states, and covers a longer range than the sensor based measurements.

Finally, surrounding vehicles detected by the onboard sensors are used to construct a vehicle trail. The idea is that vehicles traveling along the road implicitly trace its geometry by fitting a clothoid to their observed positions, a description of the road ahead can be extracted and used to update the road state. The construction of the vehicle trail is described in detail in Chapter 6.

4.4 Estimation Objective

The aim of the estimator is to recursively estimate the road geometry ahead of the host vehicle from the available onboard sensor observations. More specifically, the objective is to estimate the posterior mean and covariance of the road state vector $\mathbf{r}_k$ at each time step k.

The road state at time step k is given by (4.1), where $\mathbf{r}_k$ parameterizes the road geometry in the local vehicle fixed coordinate frame. This state contains the quantities required to describe the road ahead, such as the lateral offset, heading, curvature, segment wise curvature rates, distance to the road edges, and lane width.

Let

$$\mathbf{z}_{1:k} = \{\mathbf{z}_1, \mathbf{z}_2, \ldots, \mathbf{z}_k\}$$

denote the set of all measurements available up to time step k. Here $\mathbf{z}_k$ is used in place of $\mathbf{y}_k$ from Chapter 3 to distinguish road-specific measurements from the general filtering notation. These measurements may include observations of road features such as lane markings and road edges, moving vehicles, roadside objects, and map based road information, depending on the sensor configuration and estimation setup.

The estimation problem is then to recursively compute the posterior distribution

$$p(\mathbf{r}_k \mid \mathbf{z}_{1:k}) \tag{4.2}$$

or, under a Gaussian approximation, to estimate the corresponding posterior mean and posterior covariance,

$$\hat{\mathbf{r}}_{k|k} = \mathbb{E}[\mathbf{r}_k \mid \mathbf{z}_{1:k}] \tag{4.3}$$

and

$$\mathbf{P}_{k|k} = \mathrm{Cov}(\mathbf{r}_k \mid \mathbf{z}_{1:k}) \tag{4.4}$$

Therefore, the estimation objective is to obtain, at each time step, an estimate of the road state, depicted in Figure 4.3 as the red-dotted centerline, together with its associated uncertainty, conditioned on all measurements collected up to that time. This posterior estimate forms the basis for predicting the road geometry ahead of the host vehicle and for fusing information from multiple observation sources in a consistent Bayesian framework.

5

Process Model

This chapter describes the process model used to predict the evolution of the road state between measurement updates as the ego vehicle moves forward. Since the road geometry is represented in a local vehicle fixed coordinate frame, the process model must account both for the ego motion and for the progression along the segmented road representation.

The ego vehicle motion is treated as a known input, with the speed v_k and yaw rate $\dot{\psi}_k$ available from the onboard sensors. The distance traveled between time steps is

$$d_k = v_k \cdot \delta t. \tag{5.1}$$

This chapter focuses on the prediction part of the estimator by defining the process model, the associated process noise, the handling of adaptive segment lengths, and the resulting state prediction.

5.1 State Transition

As the ego vehicle travels forward by d_k, the road state is updated according to the nonlinear state transition model

$$\mathbf{r}_{k+1} = f(\mathbf{r}_k, \mathbf{u}_k) + \mathbf{w}_k, \qquad \mathbf{w}_k \sim \mathcal{N}(\mathbf{0}, \mathbf{Q}), \tag{5.2}$$

where $\mathbf{u}_k = [v_k,\ \dot{\psi}_k]^\top$ is the known ego motion input, $\mathbf{w}_k$ is the process noise term at time step k, and $\mathbf{Q}$ is the corresponding process noise covariance matrix. The individual state updates are derived as follows.

The lateral offset updates as the ego vehicle moves forward along the road, picking up the lateral component of its displacement:

$$y_{k+1}^{\text{off}} = y_k^{\text{off}} + \sin(\varphi_k) \cdot d_k + w_k^y. \tag{5.3}$$

The road heading state is updated by evaluating the road heading at the ego vehicle's new position, where the front axle serves as the reference point, as depicted in Figure 4.1, and subtracting the ego vehicle's change in heading over the time step:

$$\varphi_{k+1} = \varphi_r(d_k) - \dot{\psi}_k \cdot \delta t + w_k^\psi, \tag{5.4}$$

where $\varphi_r(s)$ is the road heading at arc length s, evaluated by finding which segment i contains s. Similarly, the initial curvature is updated by evaluating the road curvature at the new ego position:

$$\kappa_{0,k+1} = \kappa_r(d_k) + w_k^{\kappa}, \tag{5.5}$$

where $\kappa_r(s)$ is the road curvature at arc length s.

The road is modeled as a sequence of connected clothoid segments. For a given s, the first step is to determine which segment contains that point. Let the interval covered by segment i be defined as

$$\mathcal{A}_i^r = \left[\sum_{n=1}^{i-1} \ell^{road,n}, \sum_{n=1}^{i} \ell^{road,n}\right] \tag{5.6}$$

Here, $\ell^{\text{road},n}$ denotes the length of road model segment n, while n is a local summation index. Then, for a point $s \in \mathcal{A}_i^r$, the corresponding local arc length within segment i is given by

$$\Delta s_i = s - \sum_{n=1}^{i-1} \ell^{road,n} \tag{5.7}$$

That is, Δs_i measures the distance from the beginning of segment i to the point located at global arc length s.

The road curvature and heading at arc length s are obtained by evaluating the clothoid model of the segment whose interval contains s. Then, for $s \in \mathcal{A}_i^r$, the road curvature and heading are given by

$$\kappa_r(s) = \kappa_0^i + c^i \Delta s_i \tag{5.8}$$

and

$$\varphi_r(s) = \varphi_0^i + \kappa_0^i \Delta s_i + \frac{1}{2} c^i \Delta s_i^2 \tag{5.9}$$

where κ^i and φ_0^i denote the curvature and heading at the start of segment i, and c^i is the curvature rate of that segment.

To ensure continuity between neighboring segments, the initial curvature and heading of each segment are inherited from the preceding segment, as described in equations (2.8) and (2.9). This means that the initial curvature satisfies the recursive relation

$$\kappa_0^i = \kappa_0^{i-1} + c^{i-1} \ell^{road,i-1} \tag{5.10}$$

which can be expanded as

$$\kappa_0^i = \kappa_0^1 + \sum_{n=1}^{i-1} c^n \ell^{road,n} \tag{5.11}$$

Substituting (5.11) into (5.8) gives

$$\kappa_r(s) = \kappa_0^1 + \sum_{n=1}^{i-1} c^n \ell^{road,n} + c^i \Delta s_i, \qquad s \in \mathcal{A}_i^r \tag{5.12}$$

In other words, the curvature at s is obtained by starting from the initial curvature of the first segment, adding the curvature changes contributed by all preceding segments, and finally adding the local contribution of the current segment.

Similarly, the initial heading of segment i is obtained recursively from the preceding segments as

$$\varphi_0^i = \varphi_0^1 + \sum_{n=1}^{i-1} \left(\kappa_0^n \ell^{road,n} + \frac{1}{2} c^n \left(\ell^{road,n} \right)^2 \right) \tag{5.13}$$

and the road heading at arc length s is therefore given by

$$\varphi_r(s) = \varphi_0^i + \kappa_0^i \Delta s_i + \frac{1}{2} c^i \Delta s_i^2, \qquad s \in \mathcal{A}_i^r \tag{5.14}$$

In this way, the full road geometry is described as a piecewise sequence of connected clothoid segments. For a given global arc length s, the road geometry is obtained by first identifying the segment interval $\mathcal{A}_i^r$ that contains s, then computing the local arc length Δs_i, and finally evaluating the corresponding clothoid expressions for curvature and heading.

The curvature rates c^i, lane width w^{lane}, and road edge distances $d_k^{e_r}$ and $d_k^{e_l}$ are modeled as slowly varying:

$$c_{k+1}^i = c_k^i + w_k^{c^i}, \tag{5.15}$$

$$w_{k+1}^{\text{lane}} = w_k^{\text{lane}} + w_k^w, \tag{5.16}$$

$$d_{k+1}^{e_r} = d_k^{e_r} + w_k^{d_r}, \tag{5.17}$$

$$d_{k+1}^{e_l} = d_k^{e_l} + w_k^{d_l}, \tag{5.18}$$

where all noise terms $w_k^{(\cdot)}$ are components of $\mathbf{w}_k \sim \mathcal{N}(\mathbf{0}, Q)$.

In addition to the state updates above, the segment lengths shrink as the ego vehicle moves forward:

$$\ell_{k+1}^{road,1} = \ell_k^{road,1} - d_k. \tag{5.19}$$

When the first segment length reaches zero or below, that segment is discarded and the remaining segments are shifted forward by one index. A new segment is then appended at the far end of the road representation.

In contrast to the recursive road model formulation in (5.10) and (5.13), the map based representation provides curvature directly as a function of global arc length. Therefore, no recursive propagation of the initial curvature is required when a new segment is appended. Instead, the curvature rate of the new segment is initialized from the average rate of change of the map curvature over the segment length.

Let the interval covered by map segment i be defined as

$$\mathcal{A}_i^{\text{map}} = \left[\sum_{n=1}^{i-1} \ell^{\text{map},n}, \ \sum_{n=1}^{i} \ell^{\text{map},n} \right]. \tag{5.20}$$

For a point $s \in \mathcal{A}_i^{\mathrm{map}}$, the corresponding local arc length within map segment i is

$$\Delta s_i^{\mathrm{map}} = s - \sum_{n=1}^{i-1} \ell^{\mathrm{map},n}. \tag{5.21}$$

The map curvature as a function of global arc length is then given by

$$\kappa_r^{\mathrm{map}}(s) = \kappa_0^{\mathrm{map},i} + c^{\mathrm{map},i}\, \Delta s_i^{\mathrm{map}}, \qquad s \in \mathcal{A}_i^{\mathrm{map}}. \tag{5.22}$$

Let the global arc length at the start of the newly appended segment be defined as

$$s_{\mathrm{start}} = \sum_{n=1}^{N-1} \ell^{\mathrm{road},n}, \tag{5.23}$$

that is, as the cumulative length of the preceding segments. The global arc length at the end of the appended segment is then given by

$$s_{\mathrm{end}} = s_{\mathrm{start}} + \ell^{\mathrm{new}}, \tag{5.24}$$

where ℓ^{new} is the length of the newly appended segment, defined in (5.26). The curvature rate of the appended segment is then initialized as

$$c^N = \frac{\kappa_r^{\mathrm{map}}(s_{\mathrm{end}}) - \kappa_r^{\mathrm{map}}(s_{\mathrm{start}})}{\ell^{\mathrm{new}}}. \tag{5.25}$$

That is, the curvature rate of the appended segment is computed as the change in map curvature between s_{start} and s_{end}, divided by the segment length. Note that s_{start} and s_{end} may lie in different map segments. However, since $\kappa_r^{\mathrm{map}}(s)$ is defined as a function of global arc length, $\kappa_r^{\mathrm{map}}(s_{\mathrm{start}})$ and $\kappa_r^{\mathrm{map}}(s_{\mathrm{end}})$ are simply the map curvature values at the start and end of the appended segment.

5.1.1 Adaptive Segment Lengths

Since the map data measurements are also modeled as a sequence of segments, they can be naturally aligned with the road geometry ahead. Unlike the fixed road model representation, the map data segments have adaptive lengths that vary depending on the upcoming road characteristics. In regions with higher curvature, the segments become shorter in order to capture rapid changes in curvature and curvature rate more accurately. On the other hand, when the road ahead is relatively straight or exhibits low curvature variation, the segments become longer, since fewer geometric changes need to be represented. This adaptive segmentation enables a more efficient and accurate description of the road geometry while preserving important road features.

In addition, both a lower and an upper bound are introduced to constrain the segment lengths. The map data measurements often provide a substantially longer preview range than what is required for the road state estimation process, especially in comparison with the sensing range of the other onboard sensors. At the same time, very short segments may lead to unnecessary switching, increased sensitivity to local map variations, and reduced numerical robustness. Without such limitations, the resulting road representation could introduce unnecessary model complexity and reduce consistency between the different sensor sources. By constraining the segment lengths, the effective road representation is restricted to the region that is most relevant for the estimation problem. To align the road model segmentation with the adaptive map data segmentation, the length of the final road model segment is updated using the map data segment that best matches its longitudinal position. More specifically, the cumulative map data segment lengths are used to identify the segment whose start location is closest to the start of the final road model segment. The selected map data segment length is then blended with the nominal road model segment length according to

$$\ell^{new} = (1 - \beta)L + \beta\,\ell^{map,i} \tag{5.26}$$

where $\beta \in [0, 1]$ is a weighting factor that controls how much the road model segment length is influenced by the selected map data segment length, and $\ell^{map,i}$ denotes the map data segment that contains the starting position of the new road segment as in Equation (5.23). In the implementation, this adjustment is performed only when the ego vehicle has moved into the next segment and the road model is in the corresponding update state. The updated segment length is further restricted to remain within predefined limits, such that excessively short or long segments are avoided. In this way, the road model maintains a stable overall structure while still adapting its preview length to the road geometry described by the map data.

5.2 Process Noise

Process noise is introduced to represent uncertainty in the state evolution model and to account for effects that are not explicitly captured by the road geometry dynamics. In practice, such uncertainty may arise from unmodeled dynamics, simplifications in the road representation, slowly varying geometric changes, and errors in the ego motion inputs used in the prediction step. Process noise therefore prevents the filter from becoming overly confident in an imperfect model and allows the estimated states to adapt to real variations in the system [24].

In the state space model used in this work, the process noise covariance matrix Q is assumed to be diagonal. This implies that the process disturbances affecting the individual states are considered mutually uncorrelated. Each diagonal element is selected to reflect the expected variability of the corresponding state during a single prediction step.

The curvature rates c^i are assigned process noise to allow the road geometry to evolve over time. The lateral offset y^{off}, lane width w^{lane}, and road edge distances d^{e_r} and d^{e_l} are assigned small process noise values to capture slow variations. The heading φ_k and initial curvature $\kappa_{0,k}$ are primarily determined by the state transition function, but are also assigned process noise to account for errors in the ego motion inputs v_k and $\dot{\psi}_k$.

The values in Q are determined through manual tuning as part of the filter design process. This choice represents a trade-off between model confidence and estimator flexibility. Lower values cause the filter to follow the assumed process model more closely, while higher values make it more responsive to model mismatch, although this may increase the variability of the estimates.

5.3 Prediction Step

The prediction step is implemented using an EKF. Although the process model is nonlinear, its nonlinearity is sufficiently moderate for a first-order linearization to provide an accurate approximation during state propagation. Accordingly, since the state transition function $f(\mathbf{r}_k, \mathbf{u}_k)$ is nonlinear, the EKF prediction step requires the Jacobian of f with respect to the state $\mathbf{r}_k$, evaluated at the current state estimate $\hat{\mathbf{r}}_{k|k}$:

$$F_k = \left.\frac{\partial f}{\partial \mathbf{r}}\right|_{\hat{\mathbf{r}}_{k|k}}. \tag{5.27}$$

The Jacobian is derived by direct differentiation of the state transition Equations in (5.3) and (5.4). One key simplification is made when differentiating (5.11) and (5.13) since the sampling interval δt is small, the distance d_k traveled by the ego vehicle between two time steps will never exceed a full segment length. The ego vehicle can therefore only be located within the first or second segment at any given time step, and the summations over segments reduce to at most two terms. For the case where the ego vehicle remains within the first segment, $d_k \leq \ell_k^1$, the expressions reduce to

$$\varphi_{0,k+1} = \varphi_{0,k}^1 + \kappa_{0,k}^1 d_k + \frac{c_{1,k}^1}{2} d_k^2, \tag{5.28}$$

$$\kappa_{0,k+1} = \kappa_{0,k}^1 + c_{1,k}^1 d_k. \tag{5.29}$$

If the ego vehicle moves into the second segment, $d_k > \ell_k^1$, letting $s_1 = \ell_k^1$ and $s_2 = d_k - \ell_k^1$, the expressions become

$$\varphi_{0,k+1} = \varphi_{0,k}^1 + \kappa_{0,k}^1 s_1 + \frac{c_k^1}{2} s_1^2 + \kappa_{0,k}^2 s_2 + \frac{c_k^2}{2} s_2^2, \tag{5.30}$$

$$\kappa_{0,k+1} = \kappa_{0,k}^1 + c_k^1 s_1 + c_k^2 s_2, \tag{5.31}$$

where $\kappa_{0,k}^2$ and $\varphi_{0,k}^2$ follow from the G^2 continuity constraints in (2.8) and (2.9). Using these simplified expressions the Jacobian can be derived analytically, and the predicted state and covariance are then

$$\hat{\mathbf{r}}_{k+1|k} = f(\hat{\mathbf{r}}_{k|k}, \mathbf{u}_k), \tag{5.32}$$

$$P_{k+1|k} = F_k P_{k|k} F_k^T + Q. \tag{5.33}$$

Since the road model is represented as a sequence of segments, each defined by its length and curvature rate, the model must be updated continuously as the ego vehicle progresses along the road. To maintain a consistent representation of the estimated road geometry, the curvature rates associated with the segments are shifted as the vehicle traverses them. This ensures that the road model remains aligned with the ego vehicle's position and that the estimated road geometry evolves smoothly over time.

6

Vehicle Trail

6.1 Concept and Motivation

The road geometry is modeled as a clothoid, and all measurements entering the filter are expressed as clothoid observations. To enforce a consistent measurement structure, the contributions from moving vehicles should likewise be represented as a clothoid. Moving vehicles traveling along the road implicitly trace its geometry, and their observed positions form a trail that reflects the underlying road shape. By collecting these position samples and fitting a clothoid to them, a road geometry estimate can be extracted from surrounding traffic and used to update the filter. In Figure 4.3, this is illustrated by the red and green trails behind the surrounding vehicles.

6.2 Selection Criteria for Vehicle Trail Measurements

Not all detected moving vehicles provide reliable information about the road geometry. A set of gating criteria is therefore applied to filter out unsuitable observations before the clothoid fitting is performed.

A vehicle is admitted to the vehicle trail if all of the following conditions are satisfied:

- The vehicle speed exceeds 5 km/h, ensuring that stationary or near stationary objects are excluded.
- The vehicle is traveling in the same direction as the ego vehicle, ensuring that oncoming traffic does not corrupt the trail.
- The vehicle is observed by both camera and radar, reducing positional uncertainty through sensor fusion.
- The vehicle has been continuously observed over a distance of at least 50 m, ensuring sufficient arc length for a reliable clothoid fit.

- The observation window is capped at 70 m, beyond which older samples are discarded to maintain local relevance to the current road geometry.

6.3 Vehicle Position Propagation and Uncertainty

At each time step, a new vehicle position observation is obtained. Since each vehicle has a unique ID, a consistent trail can be maintained across time steps. To keep the trail in the current ego vehicle frame, all previously stored trail points are propagated whenever a new observation becomes available. The stored trail consists of historical points retained up to a maximum longitudinal distance of 70 m behind the ego vehicle, beyond which points are discarded.

Let the set of stored trail points at time step $k-1$ be denoted by

$$\mathcal{P}_{k-1} = \{\mathbf{p}_{m,k-1}\}_{m=1}^{M_{k-1}}, \tag{6.1}$$

where

$$\mathbf{p}_{m,k-1} = \begin{bmatrix} x_{m,k-1} \\ y_{m,k-1} \end{bmatrix} \tag{6.2}$$

is the mth trail point and M_{k-1} is the number of stored points at time step $k-1$.

The relative motion of the ego vehicle between two consecutive time steps is described by the incremental translation

$$\Delta\mathbf{p}_k = \begin{bmatrix} d_{x,k} \\ d_{y,k} \end{bmatrix}, \tag{6.3}$$

where $\Delta\mathbf{p}_k \in \mathbb{R}^2$ denotes the position increment at time step k, with components $d_{x,k}$ and $d_{y,k}$ representing the displacement in the x- and y-directions, respectively. The corresponding incremental heading change is given by

$$\Delta\psi_k = \dot{\psi}_k \delta t. \tag{6.4}$$

Each stored trail point is first translated according to

$$\tilde{\mathbf{p}}_{m,k-1} = \mathbf{p}_{m,k-1} - \Delta\mathbf{p}_k, \qquad i = 1, \ldots, M_{k-1}, \tag{6.5}$$

and is then rotated into the updated ego vehicle frame:

$$\mathbf{p}_{m,k} = \mathbf{R}(-\Delta\psi_k)\tilde{\mathbf{p}}_{m,k-1}, \qquad m = 1, \ldots, M_{k-1}, \tag{6.6}$$

where the inverse rotation matrix is defined as

$$\mathbf{R}(-\Delta\psi_k) = \begin{bmatrix} \cos(\Delta\psi_k) & \sin(\Delta\psi_k) \\ -\sin(\Delta\psi_k) & \cos(\Delta\psi_k) \end{bmatrix}. \tag{6.7}$$

In component form, the propagated coordinates become

$$x_{m,k} = \cos(\Delta\psi_k)\,(x_{m,k-1} - d_{x,k}) + \sin(\Delta\psi_k)\,(y_{m,k-1} - d_{y,k}), \qquad m = 1, \ldots, M_{k-1}, \tag{6.8}$$

$$y_{m,k} = -\sin(\Delta\psi_k)\left(x_{m,k-1} - d_{x,k}\right) + \cos(\Delta\psi_k)\left(y_{m,k-1} - d_{y,k}\right), \qquad m = 1, \ldots, M_{k-1}. \tag{6.9}$$

The incremental displacement is approximated in the local frame from the vehicle speed v_k and incremental heading change as

$$d_{x,k} = v_k \delta t \cos(\Delta\psi_k), \tag{6.10}$$

$$d_{y,k} = v_k \delta t \sin(\Delta\psi_k). \tag{6.11}$$

After propagation of the historical trail points, the newly observed vehicle position is appended to the trail in the current ego frame. Trail points whose longitudinal distance exceeds 70 m behind the ego vehicle are removed.

For each trail point, an associated covariance σ is maintained. Let the covariance of point m at time step $k-1$ be

$$\mathbf{\Sigma}_{m,k-1} = \begin{bmatrix} \sigma^2_{x,m,k-1} & \sigma_{xy,m,k-1} \\ \sigma_{xy,m,k-1} & \sigma^2_{y,m,k-1} \end{bmatrix}. \tag{6.12}$$

During propagation, the covariance is first rotated consistently with the coordinate transformation and is subsequently inflated by additive process noise to account for drift and unmodeled errors. Defining

$$c = \cos(\Delta\psi_k), \tag{6.13}$$

$$s = \sin(\Delta\psi_k), \tag{6.14}$$

the rotated covariance components are given by

$$\sigma^{2,\mathrm{rot}}_{x,m,k} = c^2\sigma^2_{x,m,k-1} - 2cs\,\sigma_{xy,m,k-1} + s^2\sigma^2_{y,m,k-1}, \tag{6.15}$$

$$\sigma^{2,\mathrm{rot}}_{y,m,k} = s^2\sigma^2_{x,m,k-1} + 2cs\,\sigma_{xy,m,k-1} + c^2\sigma^2_{y,m,k-1}, \tag{6.16}$$

$$\sigma^{\mathrm{rot}}_{xy,m,k} = (c^2 - s^2)\sigma_{xy,m,k-1} - cs\left(\sigma^2_{y,m,k-1} - \sigma^2_{x,m,k-1}\right). \tag{6.17}$$

To account for drift and unmodeled errors introduced by repeated propagation, additive process noise is included for all previously stored points. The corresponding covariance inflation is modeled by the parameters q_x and q_y, representing the longitudinal and lateral process noise variances, respectively.

The propagated covariance is then updated as

$$\sigma^2_{x,m,k} = \sigma^{2,\mathrm{rot}}_{x,m,k} + q_x, \tag{6.18}$$

$$\sigma^2_{y,m,k} = \sigma^{2,\mathrm{rot}}_{y,m,k} + q_y, \tag{6.19}$$

$$\sigma_{xy,m,k} = \sigma^{\mathrm{rot}}_{xy,m,k}. \tag{6.20}$$

Each newly appended observation is assigned an initial covariance based on its measurement uncertainty in the longitudinal and lateral directions:

$$\mathbf{\Sigma}_{\mathrm{new},k} = \begin{bmatrix} \sigma^2_{x,\mathrm{new},k} & 0 \\ 0 & \sigma^2_{y,\mathrm{new},k} \end{bmatrix}. \tag{6.21}$$

This propagation step ensures that all retained trail points remain expressed in the current ego vehicle frame, while their uncertainty is updated consistently and can subsequently be used in the weighted nonlinear least squares clothoid fit.

6.4 Clothoid Fitting via Weighted Nonlinear Least Squares

6.4.1 Measurements and Parameters

The propagated trail points and their associated covariances, as described in the previous section, are used as input to the clothoid fitting procedure. At the current time step, the propagated trail points are denoted by $\{(x_{m,k}, y_{m,k})\}_{m=1}^{M_k}$. For notational simplicity, the time index k is omitted in the following, and the samples are written as $\{(x_m, y_m)\}_{m=1}^{M}$. The associated arc length parameters are denoted by $\{s_m\}_{m=1}^{M}$. The goal is to estimate the clothoid parameter vector

$$\boldsymbol{\theta} = \begin{bmatrix} x_0 & y_0 & \varphi_0 & \kappa_0 & c \end{bmatrix}^T. \tag{6.22}$$

where (x_0, y_0) is the initial position, φ_0 the initial heading, κ_0 the initial curvature, and c the curvature rate. This is consistent with the state vector defined in Chapter 4, but is used here to describe the fitted vehicle trail rather than the road state.

Using the clothoid equations in (2.5)–(2.7), the predicted curve is described by the curvature, heading, and coordinate parametrization of each segment. As noted in Section 2.3, the coordinate integrals have no closed-form solution and are therefore approximated using a Taylor series expansion.

6.4.2 Residual Vector

For each sample m, the residual vector between the observed and predicted position is defined as

$$\mathbf{r}_m(\boldsymbol{\theta}) = \begin{bmatrix} r_{x,m}(\boldsymbol{\theta}) \\ r_{y,m}(\boldsymbol{\theta}) \end{bmatrix} = \begin{bmatrix} x_m - \hat{x}(s_m; \boldsymbol{\theta}) \\ y_m - \hat{y}(s_m; \boldsymbol{\theta}) \end{bmatrix}. \tag{6.23}$$

The full residual vector is obtained by stacking all point wise residuals:

$$\mathbf{r}_m(\boldsymbol{\theta}) = \begin{bmatrix} \mathbf{r}_1(\boldsymbol{\theta}) \\ \mathbf{r}_2(\boldsymbol{\theta}) \\ \vdots \\ \mathbf{r}_M(\boldsymbol{\theta}) \end{bmatrix}. \tag{6.24}$$

6.4.3 Weighted Nonlinear Least Squares Objective

Using the residual vector $\mathbf{r}_M(\boldsymbol{\theta})$ defined in the previous subsection, the weighted nonlinear least squares problem is written as

$$\hat{\boldsymbol{\theta}} = \arg\min_{\boldsymbol{\theta}} \sum_{m=1}^{M} \mathbf{r}_m(\boldsymbol{\theta})^T \boldsymbol{\Sigma}_m^{-1} \mathbf{r}_m(\boldsymbol{\theta}). \tag{6.25}$$

with associated covariance matrix

$$\boldsymbol{\Sigma}_m = \begin{bmatrix} \sigma_{x,m}^2 & \sigma_{xy,m} \\ \sigma_{xy,m} & \sigma_{y,m}^2 \end{bmatrix}. \tag{6.26}$$

6.4.4 Initialization

Since the residual functions $r_{x,m}(\boldsymbol{\theta})$ and $r_{y,m}(\boldsymbol{\theta})$ are nonlinear in $\boldsymbol{\theta}$, the objective function is generally non-convex and may have multiple local minima, making a good initialization important for convergence. The initial parameter vector is constructed differently depending on three cases: whether the vehicle trail starts ahead of or behind the ego vehicle, and whether a previous trail estimate is available.

The initial position is always set to the first sample of the trail:

$$x_0^{(0)} = x_1, \qquad y_0^{(0)} = y_1. \tag{6.27}$$

The remaining parameters $(\varphi_0^{(0)}, \kappa_0^{(0)}, c^{(0)})$ are initialized according to one of the following cases.

- **Case A: trail starts ahead of ego vehicle ($x_0 \geq 0$).** When the vehicle trail starts ahead of the ego vehicle, a reliable road model estimate is available. This estimate is propagated to the arc length corresponding to the first trail sample,

  $$s_0 = \sqrt{x_0^2 + y_0^2}. \tag{6.28}$$

  The heading and curvature parameters are then initialized from the road state at s_0 using Equations (2.8)–(2.9). This provides an initial guess that is close to a physically meaningful solution.

- **Case B: trail starts behind ego vehicle ($x_0 < 0$).** When the vehicle trail starts behind the ego vehicle, no reliable road model prior is available at that position. An initial heading is instead estimated from the first M_{init} samples using the average displacement between consecutive points:

$$\varphi_0^{(0)} = \text{atan2}\left(\sum_{m=1}^{M_{\text{init}}-1} (y_{m+1} - y_m), \sum_{m=1}^{M_{\text{init}}-1} (x_{m+1} - x_m) \right), \tag{6.29}$$

  where $M_{\text{init}} \in [1, M]$ denotes the number of initial trail samples used for estimating the heading, and where the curvature and curvature rate parameters are initialized from the current road model.

- **Case C: prior trail estimate available.** If a vehicle trail estimate from the previous time step is available, the shape parameters are reused with the updated initial position, providing continuity between estimates:

$$\boldsymbol{\theta}_k^{(0)} = \boldsymbol{\theta}_{k-1} \tag{6.30}$$

6.5 Lane Assignment

Before the vehicle trail can be used as a measurement, the lane in which the observed vehicle is traveling must be determined. This is necessary to establish the correct lateral offset between the vehicle trail and the road centerline. Three hypotheses are considered:

$$H_0 : \text{vehicle is in the ego lane,} \quad \delta_0 = 0, \tag{6.31}$$
$$H_1 : \text{vehicle is in the left adjacent lane,} \quad \delta_1 = w^{\text{lane}}, \tag{6.32}$$
$$H_2 : \text{vehicle is in the right adjacent lane,} \quad \delta_2 = -w^{\text{lane}}, \tag{6.33}$$

where δ_j is the lateral offset of the vehicle trail from the road centerline under hypothesis H_j.

The lane assignment is performed by comparing the initial lateral position y_0 of the fitted vehicle trail clothoid, corresponding to the first trail sample at arc length s_0, to the expected lateral position under each hypothesis.

The expected lateral position under each hypothesis is obtained by evaluating the estimated road centerline at s_0 and adding the corresponding lane offset:

$$\mu_j = \hat{y}(s_0) + \delta_j, \tag{6.34}$$

where $\hat{y}(s_0)$ is the predicted lateral position of the centerline at arc length s_0, evaluated using the Taylor series approximation from Section 2.3.

The uncertainty of μ_j is estimated by propagating the state uncertainty through the measurement function using the CKF sigma points. Let $\{\mathcal{X}^{(m)}\}$ denote the sigma points generated from the current state estimate $\hat{\mathbf{r}}$ and covariance P. The predicted lateral position is evaluated for each sigma point:

$$y^{(m)} = \hat{y}(\mathcal{X}^{(m)}, s_0), \qquad m = 1, \dots, 2n, \tag{6.35}$$

giving the predicted mean and variance:

$$\bar{y} = \frac{1}{2n} \sum_{m=1}^{2n} y^{(m)}, \tag{6.36}$$

$$\mu_j = \bar{y} + \delta_j, \tag{6.37}$$

$$\sigma_j^2 = \frac{1}{2n} \sum_{m=1}^{2n} \left(y^{(m)} - \bar{y}\right)^2. \tag{6.38}$$

This captures the contribution of all relevant states, including φ_0, κ_0, and c^i, to the uncertainty of the predicted position at s_0.

The likelihood of the initial lateral position y_0 under each hypothesis is modeled as Gaussian:

$$p(y_0 \mid H_j) = \mathcal{N}\left(y_0;\, \mu_j,\, \sigma_j^2 + \sigma_{\mathrm{y},1}^2\right), \tag{6.39}$$

where $\sigma_{\mathrm{y},1}^2$ is the lateral detection uncertainty of the observed vehicle position, given in Equation (6.19) . Assuming a uniform prior $p(H_j) = \frac{1}{3}$, the posterior probability of each hypothesis is given using Bayes's rule

$$p(H_j \mid y_0) \propto p(y_0 \mid H_j) p(H_j). \tag{6.40}$$

The most likely hypothesis is selected as

$$j^* = \arg\max_j \, p(H_j \mid y_0), \tag{6.41}$$

and the corresponding offset δ_{j^*} is used in the measurement model. If the maximum posterior probability falls below a threshold γ, the lane assignment is considered ambiguous and the vehicle trail is discarded for that time step.

6.6 Integration into the Measurement Framework

The output of the vehicle trail module is a fitted clothoid $\hat{\boldsymbol{\theta}}$, expressed in the same parametric form as the road model state vector. This makes it directly compatible with the measurement models described in upcoming Chapter 7, where it enters the filter update step as a clothoid observation. The measurement covariance is currently set manually, as the least squares fitting does not yet propagate a formal uncertainty estimate.

7

Measurement Models

This chapter describes the measurement models used in the filter. All measurement sources namely road features, map data, and vehicle trails share a common structure in which the predicted road geometry is sampled at a set of arc lengths and compared to the corresponding observed lateral positions. The resulting residuals enter the filter update step described in Section 7.5.

7.1 Input Data and Sensor Overview

All measurements used in the filter are obtained from recorded log data, providing time stamped signals from the onboard sensors and control units. The signals are preprocessed prior to use, and some include a confidence score reflecting their reliability as well as a source label indicating whether the detection originated from the camera, the radar, or a fusion of both.

Lane markings, road edges, and road barriers are provided as clothoid parametrization in the ego vehicle coordinate frame, consistent with the road model defined in Chapter 2. Since these measurements all originate at the ego vehicle position, they are described by a single clothoid segment starting ego vehicle position. For each boundary, the following quantities are available:

- Lateral offset (y^{off}): the lateral distance from the ego vehicle to the boundary,
- Heading angle (φ): the heading of the boundary relative to the ego vehicle heading,
- Curvature (κ_0): the curvature of the boundary at the ego vehicle,
- Curvature rate (c): the rate of change of curvature along the boundary.

The map data is assumed to provide a clothoid based description of the road ahead, divided into five segments. Each segment is characterized by its length $\ell^{\text{map},n}$ and curvature rate c^{map}. In addition, the curvature κ_0^{map} at the start of the current segment and the heading φ^{map} of the ego vehicle relative to the mapped path are provided. Unlike the other measurements, the map data spans multiple segments ahead and therefore covers a longer range. Since the map is fixed to the road, only the heading and the curvature of the current segment change between iterations as the ego vehicle moves forward. Segment lengths that become negative due to ego vehicle progression are treated as invalid and set to zero.

The vehicle trail, described in detail in Chapter 6, provides a clothoid fitted to the observed positions of surrounding vehicles. Unlike the other measurements, the vehicle trail does not necessarily start at the ego vehicle position, it may begin at some longitudinal distance ahead. The vehicle trail therefore provides both a longitudinal offset, indicating where ahead of the ego vehicle the fitted clothoid begins, and a lateral offset describing its lateral position in the ego vehicle frame. This distinction is important for how the vehicle trail enters the measurement model, as described in Section 6.6.

7.2 General Measurement Model

As introduced in Chapter 3 a measurement model describes how the measurement $\boldsymbol{y}_k$ is related to the current state $\boldsymbol{x}_k$. Although this dependence is causal, it is generally uncertain due to noise and modeling inaccuracies, meaning that the measurement is only an imperfect observation of the true state. This relationship is therefore modeled probabilistically using the conditional distribution of the measurement given the state, as introduced in Equation (3.1), and is denoted by $p(\boldsymbol{y}_k \mid \boldsymbol{x}_k)$ [19].

In this work, all measurement sources are processed according to a common procedure. For each observation, a valid longitudinal interval is first defined from the measured start position and its associated valid range. This interval is then discretized into N_{sample} arc length positions, uniformly spaced along the observation. For each sampled arc length s_j^{sample}, with $j = 1, \ldots, N_{\text{sample}}$, the corresponding road segment is identified, and the local arc length within that segment is computed using Equation (5.7). The geometric conditions at the start of the identified segment, namely position, heading, and curvature, are then evaluated using Equations (2.8), (2.9), and (2.10). These quantities define the local clothoid segment associated with the current road state estimate.

Before evaluating the clothoid approximation, a lateral offset associated with the measurement is added to the road state. For lane markings, the offset is given by

$$\pm \frac{w^{\text{lane}}}{2}, \tag{7.1}$$

and for road edges by

$$d^{e_j}. \tag{7.2}$$

For other measurement types, the lateral offset is taken directly from the measurement itself.

To compare an observation with the current road state estimate, both are evaluated at the same set of sampled arc lengths s_j^{sample}, with $j = 1, \ldots, N_{\text{sample}}$. For each sample point, the road model provides a predicted lateral coordinate

$$H(s_j^{\text{sample}}; \boldsymbol{r}_k), \tag{7.3}$$

while the measurement source provides the corresponding measured lateral coordinate

$$y(s_j^{\text{sample}}). \tag{7.4}$$

The predicted coordinates are obtained by evaluating the clothoid approximation described in Section 2.3 at the sampled arc lengths. Stacking the predicted coordinates over all sample points gives the predicted measurement vector

$$\hat{\boldsymbol{y}}_k = \Big[H(s_1^{\text{sample}}; \boldsymbol{r}_k) \quad \ldots \quad H(s_{N_{\text{sample}}}^{\text{sample}}; \boldsymbol{r}_k)\Big]^T, \tag{7.5}$$

and stacking the measured coordinates in the same way gives

$$\boldsymbol{y}_k^{\text{meas}} = \Big[y(s_1^{\text{sample}}) \quad \ldots \quad y(s_{N_{\text{sample}}}^{\text{sample}})\Big]^T. \tag{7.6}$$

The residual vector is then defined as the difference between measurement and prediction,

$$\boldsymbol{\nu}_k = \boldsymbol{y}_k^{\text{meas}} - \hat{\boldsymbol{y}}_k. \tag{7.7}$$

Thus, each component of $\boldsymbol{\nu}_k$ represents the lateral mismatch between the observation and the current road state estimate at one sampled arc length.

Under the assumed additive measurement model,

$$\boldsymbol{y}_k^{\text{meas}} = \hat{\boldsymbol{y}}_k + \boldsymbol{\eta}_k, \tag{7.8}$$

where $\boldsymbol{\eta}_k \sim \mathcal{N}(\boldsymbol{0}, R_k)$, the residual is modeled as an instance of the measurement uncertainty. This residual vector is used in the CKF update step described in Subsection 3.1.3.

7.3 NIS Tuning and Gating

Each measurement source is assigned a covariance matrix R that characterizes its uncertainty. These covariance matrices are not derived directly from sensor specifications, but are instead tuned manually as part of the filter design. The assigned measurement uncertainty is distance dependent, such that measurements obtained at larger distances are associated with higher uncertainty. In addition, road features such as lane markings, road edges, and barriers are typically accompanied by a confidence score. This confidence is also taken into account when tuning the measurement covariance, so that features with lower confidence are assigned higher uncertainty.

The tuning is guided by the normalized innovation squared (NIS) statistic, described in Subsection 3.1.4. Under a correctly specified measurement noise model, the NIS is expected to follow a chi-squared distribution. The covariance matrices are therefore adjusted until the resulting NIS values are statistically consistent with this distribution. This provides a principled criterion for assessing whether the assigned measurement uncertainties are well calibrated.

Once the measurement covariances have been tuned and the NIS exhibits the expected chi-squared behavior, a gating criterion is applied. Measurements whose NIS values exceed the upper 97.5% chi-squared bound are regarded as ambiguous or inconsistent with the current road state estimate and are therefore rejected.

7.4 Map Data Gating

To improve the robustness of the map data measurements, a gating strategy is introduced by enforcing geometric consistency with the current road state estimate. The estimated road geometry, represented by a clothoid approximation, is used as a reference for the predicted road ahead. In the implemented method, this reference is given by the estimated road centerline. The map data is then compared with this reference over the road section for which both sources provide geometry information.

The gating acts as a geometric consistency check that ensures that only measurements aligned with the estimated road centerline are used in the update step. In addition, the gating rejects measurements whose local shape development differs significantly from that of the estimated road, as such measurements could introduce inconsistencies into the filter. Before the update step, both the estimated road centerline and the map data clothoid are sampled at a common set of arc lengths within their shared valid range, enabling a direct point-by-point comparison. The map data is accepted only if its maximum absolute lateral deviation from the estimated centerline remains below a predefined threshold and if its slope evolution is consistent with that of the reference path. Measurements that do not satisfy both of these conditions are rejected as inconsistent with the current road estimate.

$$\max\left(|\mathbf{y}_{\text{map}} - \mathbf{y}_{\text{road}}|\right) < \rho_{\text{pos}}, \qquad \operatorname{mean}\left(|\mathbf{m}_{\text{map}} - \mathbf{m}_{\text{road}}|\right) < \rho_{\text{slope}} \tag{7.9}$$

Here, $\mathbf{y}_{\text{map}}$ and $\mathbf{y}_{\text{road}}$ denote the sampled lateral positions of the map centerline and the estimated road centerline at the common points, respectively, while $\mathbf{m}_{\text{map}}$ and $\mathbf{m}_{\text{road}}$ denote the corresponding local slopes. The threshold ρ_{pos} defines the maximum allowable lateral deviation, and ρ_{slope} defines the maximum allowable mean slope difference for the map data to be accepted.

7.5 Update step

The measurement update is performed using a CKF, since the measurement models exhibit stronger nonlinearities than the process model. This avoids relying solely on first-order linearization in the update step and provides a more suitable treatment of the nonlinear measurement models. Following the CKF framework presented in Chapter 3, the update step incorporates the available measurements into the predicted road state estimate in order to reduce the prediction uncertainty and improve the representation of the road geometry. Sources for which no valid measurement is available, either due to sensor unavailability or rejection by the NIS gate or map data gate, are skipped entirely and the predicted state is carried forward unchanged.

For each available source, the nonlinear measurement function $h(\cdot)$ is the clothoid evaluation described in Section 7.2. The CKF sigma points are propagated through this function at the sampled arc length positions s_j^{sample}, producing the predicted measurement vector $\hat{\mathbf{y}}_k$. The residual $\boldsymbol{\nu}_k = \mathbf{y}_k^{meas} - \hat{\mathbf{y}}_k$ is then used to correct the predicted state and covariance according to the CKF update equations derived in Section 3.1.3.

8

Results

This chapter presents the results obtained using the proposed road estimation framework. First, the experimental setup is described in Section 8.1, including the data, scenarios, and evaluation procedure. The main filter results are then presented in Section 8.2 for two representative driving environments: a highway scenario in Subsection 8.2.1 and four snow-covered rural scenarios in Subsections 8.2.2 - 8.2.5. In addition, a separate evaluation of vehicle trails is provided in Section 8.3 to assess their contribution to the road estimation process. Finally, the effect of using dynamic segment lengths is presented in Section 8.4.

8.1 Experimental Setup

The filter is evaluated on multiple driving scenarios using the same parameter setup throughout.

The first scenario is a highway scenario representing the best case condition, where all measurement sources are available. This scenario is used to evaluate the contribution of each measurement source by running the filter with different subsets of measurements and comparing the resulting estimation accuracy. The NIS gating is also evaluated on this scenario. The filter is then evaluated on more challenging driving conditions, specifically snowy rural road with varying road condition. In these scenarios the availability of measurements varies, and only the overall estimation performance is evaluated. Since no ground truth is available, the road centerline is instead estimated from the available sensor data. The ego vehicle path is first reconstructed by integrating the vehicle speed and heading over time, essentially dead reckoning, as explained in Section 2.4. At each time step, the lateral distances to the left and right lane markings are used to estimate the centerline as their mean. If one side is unavailable, the most recent lane width is used. While this reference is not true ground truth, the lateral distances from lane markings are generally reliable when available and provide a reasonable approximation of the road centerline for evaluation purposes. In addition, the vehicle trail will be evaluated separately to showcase the performance, also the dynamic segment lengths based on map data.

8.1.1 Parameter Settings

The filter configuration used throughout the experiments is summarized in the following tables, including the initialization settings, process noise parameters, and measurement uncertainties. For the segment wise road model, a nominal segment length of $L = 40$ m and a total of $N = 5$ segments were used in all evaluated scenarios.

Table 8.1: Process noise standard deviations used to construct the covariance matrix Q.

State	Value	Unit	Parameter
y^{off}	0.1	m	Lateral position
φ	0.1	$^\circ$	Heading angle
κ	1×10^{-7}	m^{-1}	Curvature
$c^1, \dots, c^N$	2×10^{-10}	m^{-2}	Curvature rate for each segment
w^{lane}	0.002	m	Lane width
d^{e_l}, d^{e_r}	0.2	m	Distance to road edge

Table 8.2: Initialization of the state estimate $\hat{\boldsymbol{r}}_{0|0}$.

State	Initialization	Unit
y_0^{off}	$(l_0^0 + r_0^0)$	m
φ_0	$0.5\,(l_0^1 + r_0^1)$	rad
κ_0	$0.5\,(l_0^2 + r_0^2)$	m^{-1}
c_0^1	$0.5\,(l_0^3 + r_0^3)$	m^{-2}
$c_0^2, \dots, c_0^N$	0	m^{-2}
w_0^{lane}	$l_0^0 - r_0^0$	m
d^{e_l}	$l_0^{e,0}$	m
d^{e_r}	$r_0^{e,0}$	m

Here, l and r represent the left and right lane markings and l^e and r^e, respectively, and the subscript 0 denotes the initialization step. The superscript identifies the associated geometric quantity, where ^{0} corresponds to lateral distance, ^{1} to heading angle, ^{2} to curvature, and ^{3} to curvature rate.

Table 8.3: Initial standard deviations used to construct the covariance matrix $P_{0|0}$.

State	Value	Unit
y^{off}	0.4	m
φ	1.5	$^\circ$
κ	0.001	m^{-1}
$c^1, \dots, c^N$	1×10^{-5}	m^{-2}
w^{lane}	0.2	m
d^{e_l}, d^{e_r}	0.4	m

Table 8.4: Lateral measurement noise standard deviation models used for the different measurement sources.

Measurement source	Standard deviation model	Parameters
Lane markings	$\sigma_y = (0.1 + 0.00012\,p^2)\,\mathrm{conf}^{-2}$	$p \in [0, \mathrm{validRange}]$
Road edges	$\sigma_y = (0.2 + 0.0004\,p^2)\,\mathrm{conf}^{-2}$	$p \in [0, \mathrm{validRange}]$
Raised barriers	$\sigma_y = (0.1 + 0.0006\,p^2)\,\mathrm{conf}^{-2}$	$p \in [0, \mathrm{validRange}]$
Map data	$\sigma_y = 0.8 + (p/20)$	$p \in [0, \mathrm{validRange}]$
Vehicle trails	$\sigma_y = 1.5 + [1,\ 1.5,\ 2,\ 2.5]\,(x_0/65)$	Depends on x_0

Here, σ_y denotes the lateral measurement standard deviation, p denotes the longitudinal position of the sampled measurement point within the valid measurement range, conf is the associated measurement confidence, and x_0 denotes the longitudinal starting position used in the vehicle trail uncertainty model.

8.2 Filter Performance Across Different Scenarios

8.2.1 Highway Scenario

The filter was initially tested on the highway scenario, as shown in Figure 8.1. The results in Figure 8.2 indicate that the RMSE decreases when additional measurement sources are incorporated. The measurement availability for the highway scenario, shown in Figure 8.3, is high for all measurements except barriers. Additionally, the NIS plots are provided in Appendix A.

Figure 8.1: Snapshot of the tested highway scenario under good conditions.

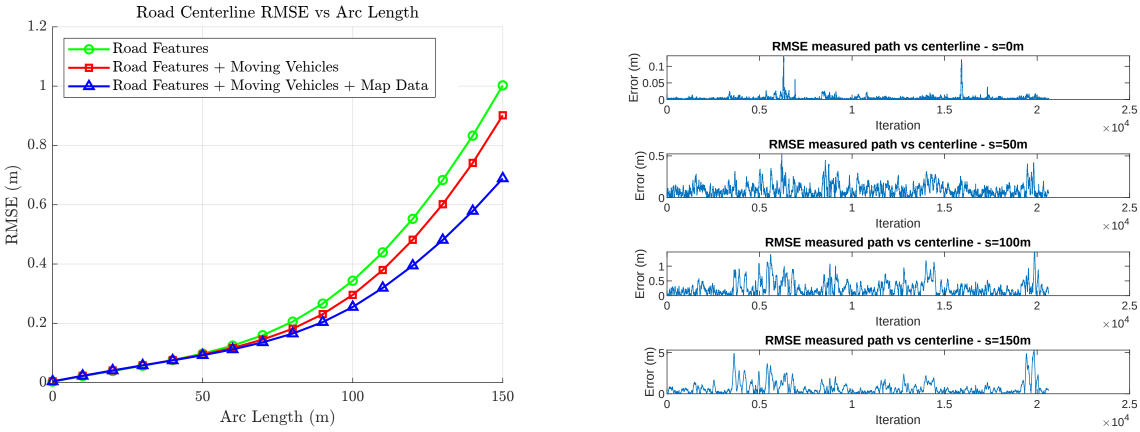

(a) Mean RMSE. **(b)** RMSE at selected distances.

Figure 8.2: RMSE evaluation for the highway scenario, comparing road features only, namely lane markings, road edges, and barriers, road features combined with moving vehicles, and all measurement sources, as well as RMSE over time at selected distances using all measurement sources.

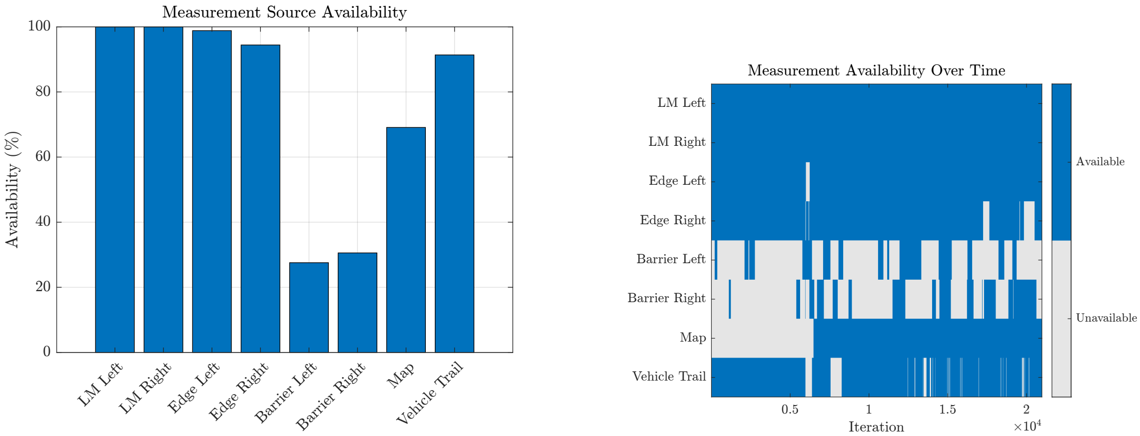

(a) Overall availability. **(b)** Availability over time.

Figure 8.3: Measurement availability analysis for the highway scenario, showing availability over the highway scenario and over time.

For the highway lane scenario, the vehicle trail classification can be observed in Figure 8.4, where the model demonstrates high accuracy in identifying the correct lane.

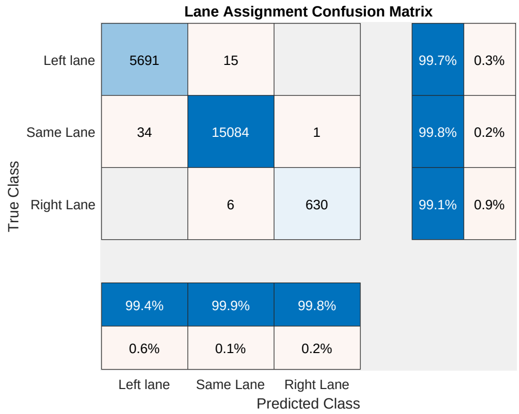

Figure 8.4: Confusion matrix comparing the true lane class with the predicted lane class for left lane, same lane, and right lane.

8.2.2 Snow-Covered Rural Scenario 1

Next, the filter was evaluated in a snow-covered rural scenario, as shown in Figure 8.5. The results in Figure 8.6 show that the RMSE increases markedly with distance, and the over time plot shows several significant spikes. The measurement availability shown in Figure 8.7 indicates low availability of map data and barriers, with no vehicle trails.

Figure 8.5: Snow-covered rural scenario 1 with mostly clear centerline but snow covering road edges and right lane marking.

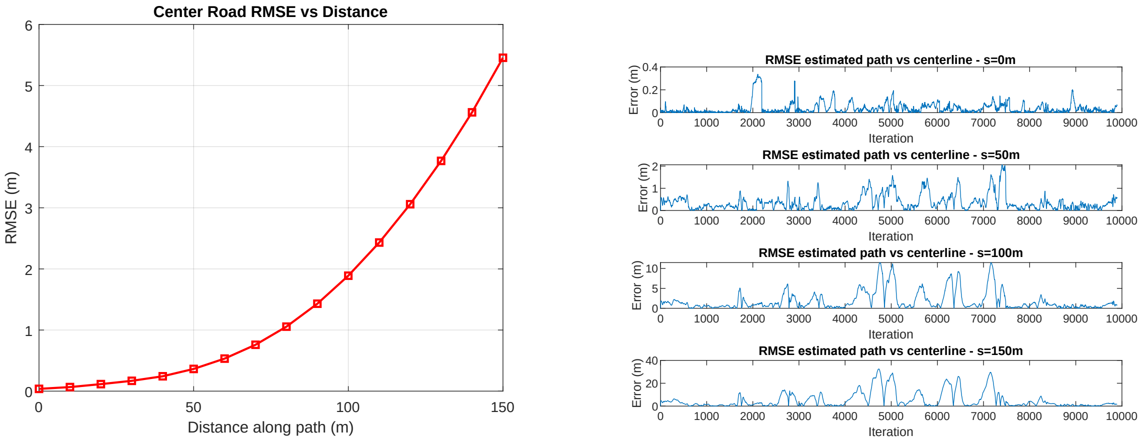

(a) Mean RMSE. **(b)** RMSE at selected distances.

Figure 8.6: RMSE evaluation for snow-covered rural scenario 1.

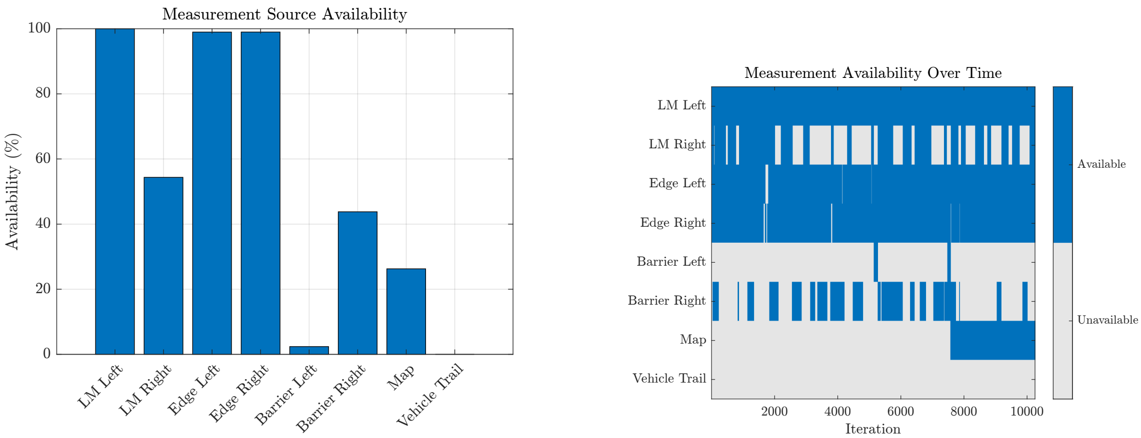

(a) Overall availability. **(b)** Availability over time.

Figure 8.7: Measurement availability analysis for snow-covered rural scenario 1.

8.2.3 Snow-Covered Rural Scenario 2

Another similar scenario was also evaluated, as shown in Figure 8.8. This time, the availability of vehicles and map data was significantly higher, as shown in Figure 8.10. The RMSE plots in Figure 8.9 show a slight increase at longer distances. The over time RMSE plot shows some spikes, but they are not as severe.

Figure 8.8: Snow-covered rural scenario 2 with partially faded lane markings and snow-covered road edges.

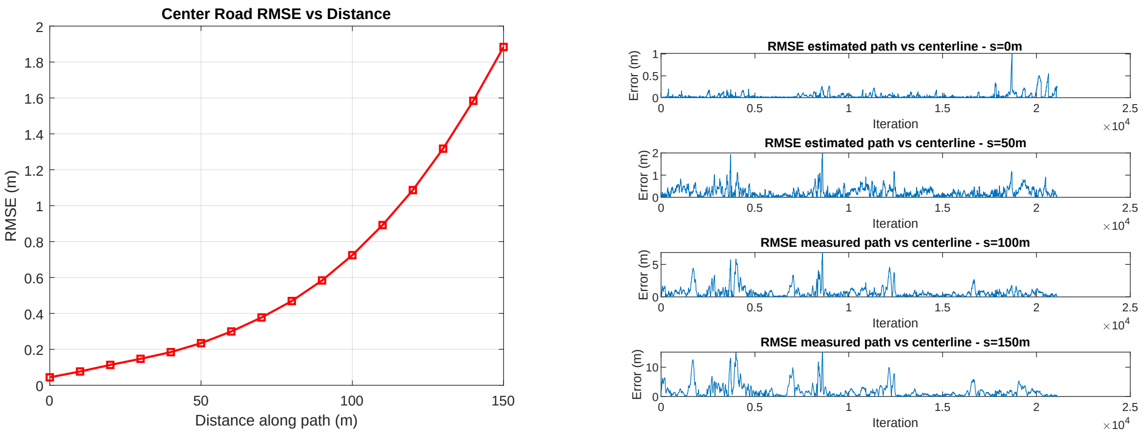

(a) Mean RMSE.

(b) RMSE at selected distances.

Figure 8.9: RMSE evaluation for the snow-covered rural scenario 2.

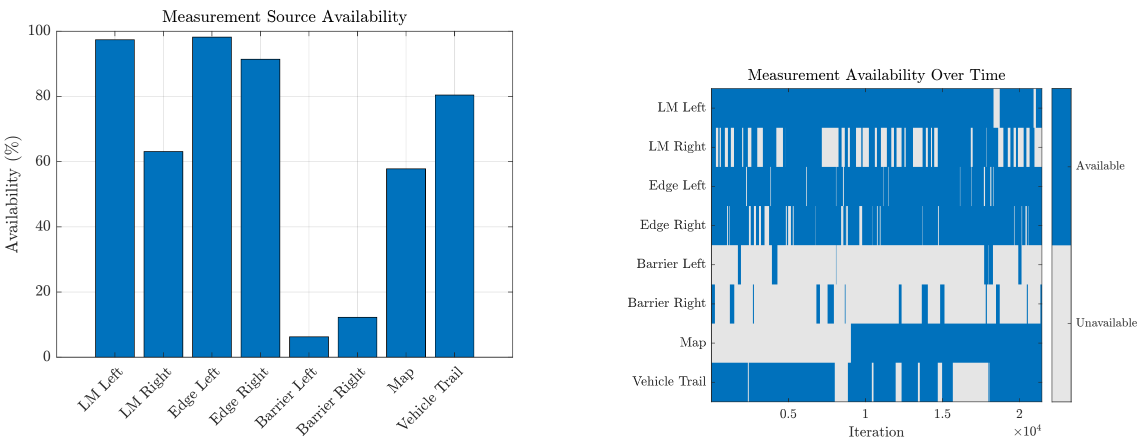

(a) Overall availability.

(b) Availability over time.

Figure 8.10: Measurement availability analysis for the snow-covered rural scenario 2.

8.2.4 Snow-Covered Rural Scenario 3

The next scenario, similar to the previous ones, was also evaluated under conditions where lane markings and road edges were almost completely covered by snow, as shown in Figure 8.11. The RMSE in Figure 8.12 indicates high error across all distances. The availability plot in Figure 8.13 shows low availability for all measurements.

Figure 8.11: Snow-covered rural scenario 3 with snow-covered lane markings and road edges.

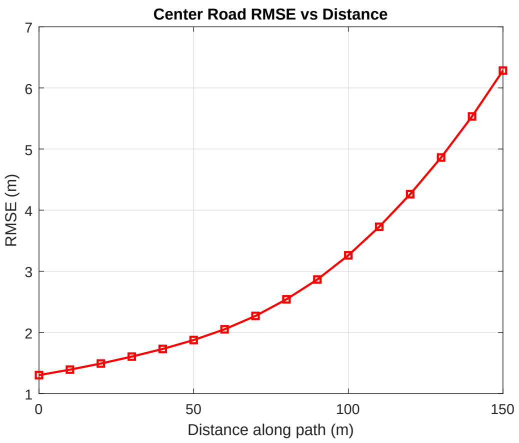

(a) Mean RMSE.

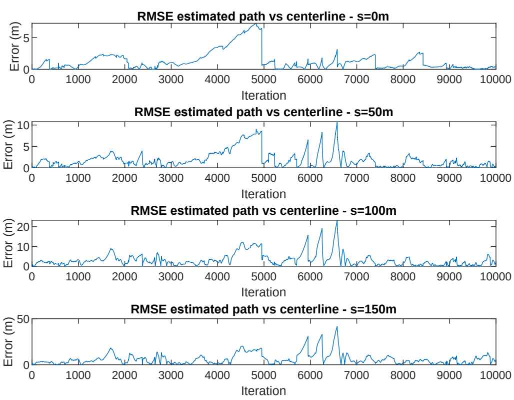

(b) RMSE at selected distances.

Figure 8.12: RMSE evaluation for the snow-covered rural scenario 3.

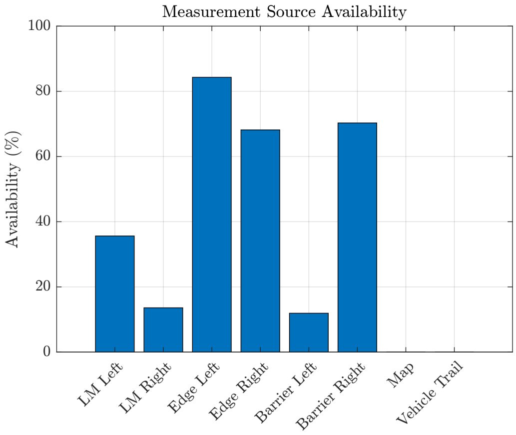

(a) Overall availability.

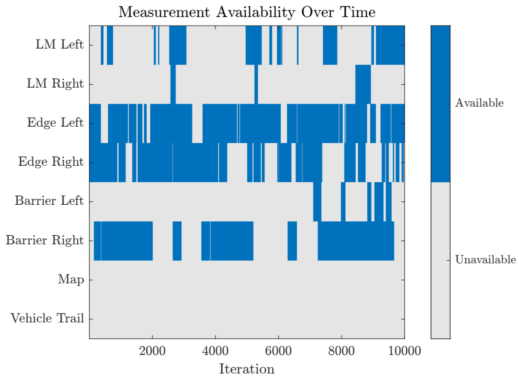

(b) Availability over time.

Figure 8.13: Measurement availability analysis for the snow-covered rural scenario 3.

8.2.5 Snow-Covered Rural Scenario 4

The last tested scenario was another snow case with partially covered lane markings, as shown in Figure 8.14. As illustrated by the availability plot in Figure 8.16, the right lane marking has very low availability as well as the vehicle trail and the barriers. The RMSE in Figure 8.15 shows low error at all distances and remains consistent over time.

Figure 8.14: Snow-covered rural scenario 4 with partially snow-covered lane marking and road edges.

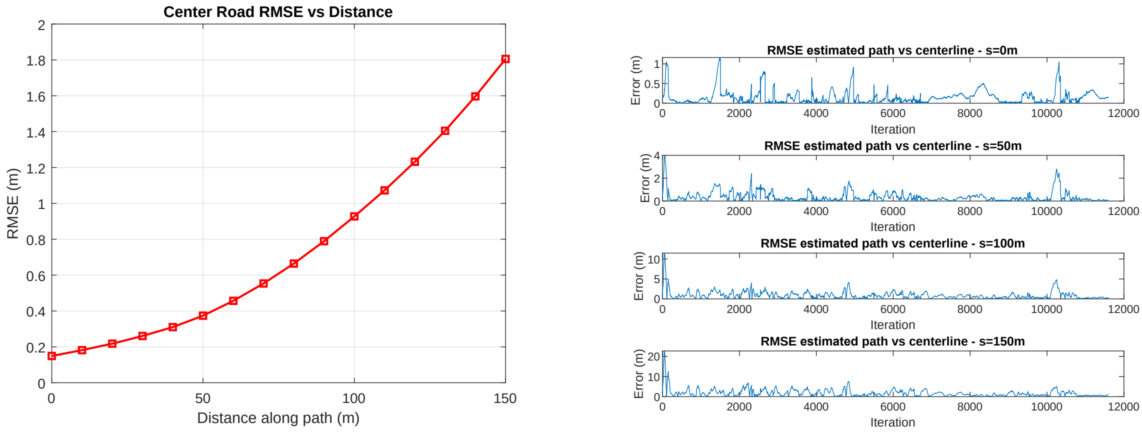

(a) Mean RMSE.

(b) RMSE at selected distances.

Figure 8.15: RMSE evaluation for the snow-covered rural scenario 4.

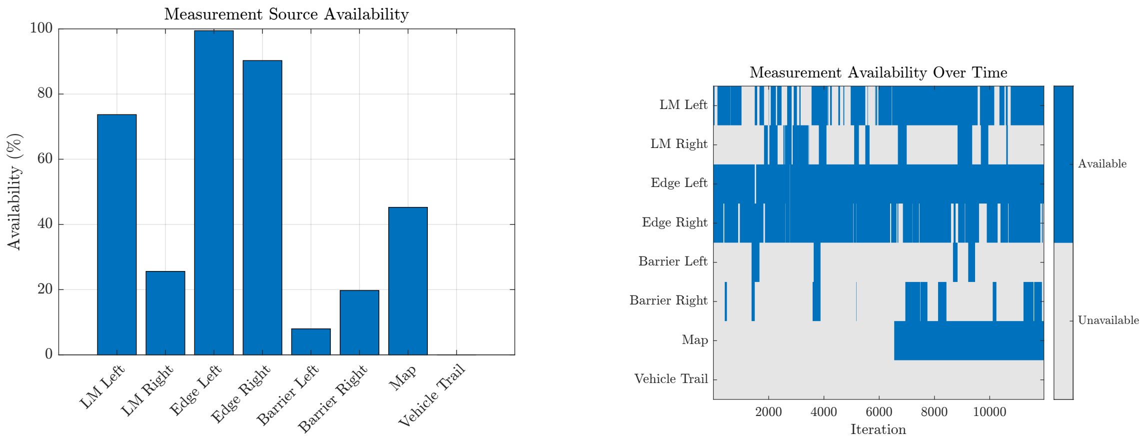

(a) Overall availability.

(b) Availability over time.

Figure 8.16: Measurement availability analysis for the snow-covered rural scenario 4.

8.3 Vehicle Trail Scenario

The vehicle trail following method was evaluated using data collected on a rural road with varying curvature see Figure 8.17 for reference. Only the vehicle trail following information was used in this evaluation, without additional measurements sources. The recorded log contains a leading vehicle at all times, with the longitudinal distance to the host vehicle varying between 40 and 90 m.

Figure 8.17: Scenario for vehicle trail following.

As shown in Figure 8.18, the RMSE remains relatively consistent up to 80 meters before increasing at greater distances. Over time, the RMSE shows an overall steady error level, particularly at distances below 50 m and at 0 m.

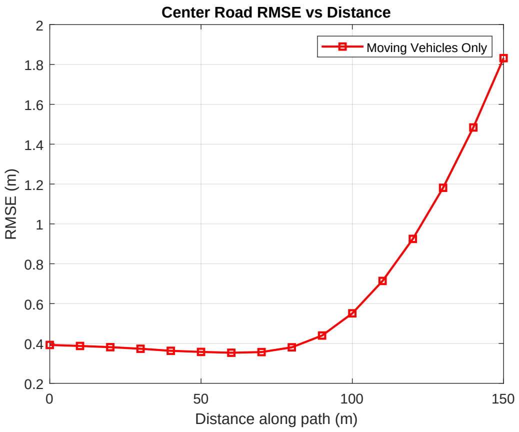

(a) Mean RMSE.

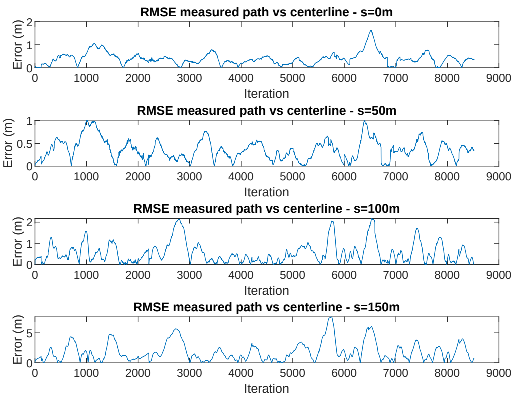

(b) RMSE at selected distances.

Figure 8.18: RMSE evaluation using vehicle trail as the only measurement.

8.4 Dynamic Segment Lengths

The dynamic segment length method was evaluated in several scenarios with high availability of map data, since map data measurements are required for segment length adaptation. The weighting factor used to combine the road model and map data segment lengths was set to $\beta = 0.5$, while the lower and upper bounds on the map data segment lengths were set to 35m and 75m, respectively. The effect of this adaptive segmentation strategy on the segment structure and estimation accuracy is presented in the following results.

Figure 8.19 shows the total segment length for both methods. For the dynamic method, the total segment length is sometimes shorter, but in most cases longer than for the static method. The mean RMSE in Figure 8.20 is similar for both methods, and no clear difference can be observed. Figure 8.21 shows the segment length as a function of road curvature. The plot indicates that the mean segment length decreases as the absolute road curvature increases.

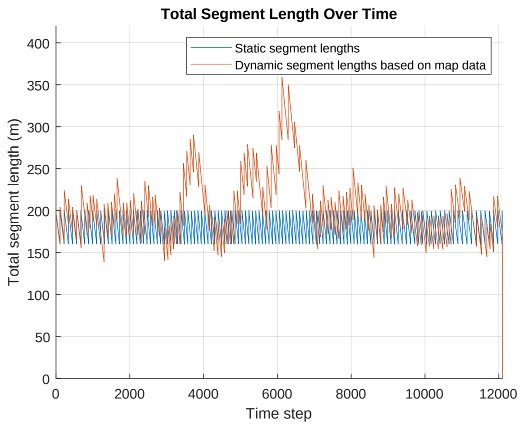

Figure 8.19: Comparison of total segment length over time using dynamic and static segment lengths.

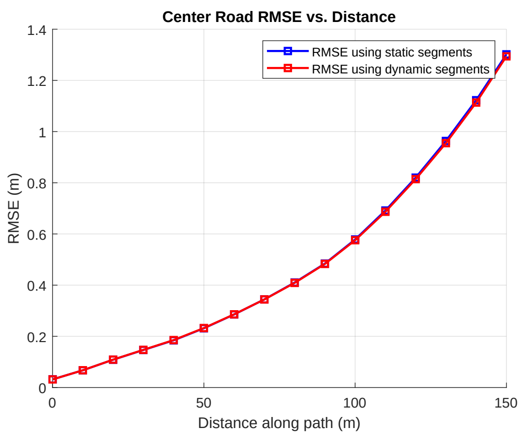

Figure 8.20: Comparison of mean RMSE using dynamic and static segment lengths.

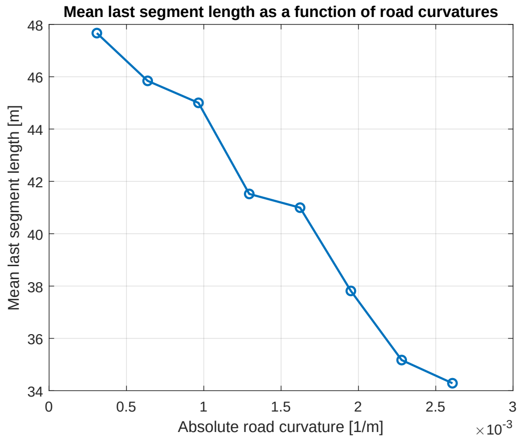

Figure 8.21: Mean length of last segment as a function of road curvature

9

Discussion

9.1 Overall Filter Performance

Figure 8.2 shows the centerline RMSE for three different measurement configurations: using only road features, using road features together with moving vehicles, and using all available measurements including map data. As shown in the Figure, the RMSE decreases as additional measurement sources are included. This indicates that the estimated road centerline geometry benefits from combining complementary sources of information. When only road features are used, the filter relies on a more limited description of the road ahead. By including moving vehicles, additional information about the road geometry becomes available, which improves the estimate and reduces the RMSE. When map data is also included, the filter has access to an even richer set of measurements, resulting in the lowest RMSE among the three cases.

This effect is particularly visible at longer distances. At an arc length of 50 m, the filter performs similarly regardless of the measurement configuration. Beyond this point, however, the difference in accuracy between the cases increases with distance. This suggests that the benefit of combining multiple measurement sources becomes more important further ahead, where the road geometry is more difficult to estimate accurately from a limited set of road feature measurements, as these typically provide reliable information only over a shorter range. The result suggests that the filter performs best when all available measurement sources are used together. This is reasonable, since each source contributes information from a different perspective, and their combination provides a more complete description of the road geometry ahead.

The NIS analysis plots in Appendix A and B present the NIS distributions for the highway scenario described in Section 8.2.1 and the snow-covered rural scenario 2 described in Section 8.2.3.

For the highway scenario, the NIS distribution closely follows a chi-squared distribution but tends to fall slightly below it. This is likely attributable to the generally high measurement quality characteristic of highway driving, which results in a filter that is marginally conservative. In contrast, the snow-covered rural scenario exhibits a considerably higher NIS distribution, which is expected given the increased measurement noise under those conditions. Importantly, however, excessive overconfidence in the filter should be avoided, as this risks the gating criterion rejecting measurements that would otherwise be informative.

The vehicle trail NIS warrants separate consideration, as it tends to be elevated relative to the other measurement sources, particularly in the highway scenario. This elevation is not a result of overconfident tuning, but rather reflects the nature of vehicle trail measurements themselves. Surrounding vehicles on highways frequently perform lane changes or take exits and forks, meaning their trajectories often do not correspond to the road ahead. The higher NIS values therefore indicate that a large proportion of vehicle trail measurements are correctly identified as inconsistent with the current road geometry and rejected by the gating criterion. When vehicle trail measurements do pass the gate, however, they are highly informative, which is why the measurement noise is still tuned to be relatively tight despite the high overall NIS.

9.2 Performance Analysis Across Scenarios

9.2.1 Highway Scenario

Figure 8.3 shows that the highway scenario provides a rich set of measurements that can be used to correct the predicted state estimate. In comparison with the measurement availability shown in Figures 8.7, 8.10, 8.13, and 8.16, the highway scenario offers substantially stronger measurement support for the filter. This difference is directly reflected in the RMSE shown in Figure 8.2, where the estimation error remains below 0.7 m even at a look-ahead distance of 150 m. The lane assignment confusion matrix in Figure 8.4 shows that the method performs as intended, with an overall lane assignment accuracy above 99%. This indicates that the algorithm can determine with high reliability whether a surrounding vehicle belongs to a specific lane relative to the detected lane markings. The low number of misclassifications suggests that lane assignment errors are rare, which demonstrates the robustness of the proposed approach under the evaluated conditions. This is important because accurate lane association of surrounding vehicles is a prerequisite for incorporating the vehicle trail correctly in the update step.

9.2.2 Snow-Covered Rural Scenarios

Comparing scenarios 8.5 and 8.8, both depict snow-covered rural roads with faded or absent lane markings, resulting in similarly challenging perception conditions. A key distinction between the scenarios lies in the measurement availability over time, as illustrated in Figures 8.7 and 8.10. Both scenarios exhibit comparable lane marking availability, characterized by a nearly continuous left lane marking and only occasional observations of the right lane marking.

However, scenario 8.8 benefits from more extensive map data coverage than scenario 8.5, which contributes to improved estimation accuracy, particularly at longer ranges. Furthermore, Figure 8.10 shows that vehicle trail measurements are available throughout parts of scenario 8.8. These additional measurements provide valuable information about the road geometry and contribute to the lower RMSE observed in Figure 8.9 compared to Figure 8.6.

This comparison indicates that, even under similarly challenging winter conditions, variations in measurement availability can significantly affect estimation performance. In particular, the presence of vehicle trail measurements, together with extended map data availability, improves the filter's ability to constrain the road centerline, leading to reduced estimation error.

In Figure 8.11, most of the road surface is covered by snow, no surrounding vehicles are present, map support is unavailable, and the lane markings are barely visible. As shown in Figure 8.13, the filter struggles to accurately estimate the road centerline under these conditions, particularly at longer distances. This behavior is expected, as the available measurements are both sparse and degraded, making reliable centerline estimation more challenging. Overall, these results suggest that road edge measurements alone provide limited support for accurate road centerline estimation in severe winter conditions.

A comparison with the scenario shown in Figure 8.14 is particularly informative, as the two scenarios appear similar at first glance. However, Figures 8.13 and 8.16 reveal notable differences in measurement availability. In the scenario shown in Figure 8.14, both lane markings are detected more consistently, particularly the left lane marking, providing stronger constraints on the road geometry. Furthermore, Figure 8.16 shows that map data becomes available during the second half of the scenario, further improving the road centerline estimation. These additional measurements contribute to the lower estimation error observed in the corresponding RMSE results.

9.3 Vehicle Trail Evaluation

In this scenario, see Figure 8.17, the vehicle trail is used as the only measurement source in the update step. As illustrated in Figure 8.18, the RMSE reaches its minimum in the area of the target vehicle and increases with distance from that location. This pattern indicates that the road centerline estimate is most accurate where direct vehicle trail information is available. Near the target vehicle, the filter receives direct measurement support from the vehicle trail, which constrains the estimate and reduces the error. As the distance from the vehicle increases, this measurement support weakens, and the estimate becomes increasingly dependent on prediction rather than correction. Consequently, uncertainty grows, which is reflected in the rising RMSE. This trend is expected because no additional measurement sources are available to reinforce the estimate outside the local region covered by the vehicle trail. Without such complementary information, small local errors can propagate and lead to larger deviations at greater distances from the measured position. Overall, the result suggests that the vehicle trail method provides reliable local support for the road centerline estimate, even when used as the only measurement source.

9.4 Dynamic Segment Lengths

Figures 8.19, 8.20, and 8.21 illustrate the effect of using dynamic segment lengths in the road model. As shown in Figure 8.19, the dynamic segmentation approach allows the segment lengths to vary compared with the static case. In practice, this results in both shorter and longer segments, although the increase in segment length appears more pronounced overall. This indicates that the method adapts the segment structure depending on the local road geometry instead of relying on a fixed nominal segment length throughout the road. The fact that longer segments occur more frequently than shorter ones suggests that the evaluated log contains a relatively large proportion of straight or only mildly curved road sections. In such parts of the road, the geometry changes slowly, which allows the model to use longer segments without compromising geometric accuracy.

Figure 8.21 shows that the length of the last segment decreases as the road curvature increases. This behavior is consistent with the intended design of the method. In regions with higher curvature, the road geometry changes more rapidly, which motivates the use of shorter segments in order to represent the shape more accurately. In straighter sections, where the geometry varies more slowly, longer segments can be used without introducing large modeling errors. The result therefore suggests that the adaptive segmentation captures the expected relationship between road curvature and required model resolution. However, the effect of this adaptation on the estimation accuracy appears limited. As shown in Figure 8.20, the RMSE obtained with dynamic segment lengths is very similar to that obtained with static segment lengths, with only minor differences between the two curves. This indicates that, under the evaluated conditions, the dynamic adjustment of the segment length has little impact on the overall estimation error.

One possible interpretation is that the baseline segment length is already sufficiently suitable for most of the evaluated road sections, such that further adaptation only produces a marginal improvement. At the same time, the dynamic method still demonstrates that the model structure can be adjusted in a geometrically meaningful way, even if this does not translate into a clearly visible RMSE reduction in the present evaluation. A further limitation is that the dynamic segment length method depends on the availability of map data measurements, since the segment adaptation is derived from the map information. As a result, the method can only be applied when such measurements are available. This can be seen in Figure 8.7, where the dynamic segment length method would only be active during part of the simulation. This limitation would be particularly relevant in rural scenarios, where map data may be sparse or less frequently updated. In such cases, the opportunity to adapt the segment structure would be reduced, which would also limit the practical benefit of the method.

A practical consideration when using dynamic segment lengths is that the chosen segmentation strategy may depend on how far ahead the road geometry is intended to be estimated. If the goal is to estimate the road geometry over a longer distance ahead of the vehicle, longer segments may be beneficial for covering a larger portion of the road, whereas shorter segments may be preferable when a more detailed local description is required.

10

Conclusion and Future Work

10.1 Conclusion

This thesis investigated road geometry estimation using a clothoid based state estimator, fusing multiple measurement sources through a nonlinear Kalman filter with statistical gating.

Regarding the first research question, the results demonstrate that incorporating map data and surrounding vehicle observations as additional measurement sources meaningfully improves the road geometry estimate compared to relying on road features alone. This improvement is most pronounced at longer ranges, where road feature detections become sparse and unreliable. Map data proved to be the most informative supplementary source, providing reliable geometric constraints across a range of conditions. Surrounding vehicle observations also contributed valuable information, particularly when their trajectories were consistent with the road ahead, effectively extending the observable horizon beyond what road features alone can provide. However, incorporating these sources requires careful handling and robust gating, as they can be highly informative but also degrade the estimate if not properly managed. Surrounding vehicles may deviate from the road ahead due to lane changes or exits, and map data may be misaligned with the actual road geometry. Both individual gating, applied per measurement source, and statistical gating through NIS consistency checks therefore play an important role in ensuring that only reliable measurements are incorporated into the estimate.

Regarding the second research question, the filter demonstrated reasonable robustness under difficult driving conditions. When only road features were available, such as in snowy conditions where detections are degraded, it was still possible to maintain an estimate of the road centerline at shorter ranges. However, when the road is fully covered by snow, road features alone are not sufficient to maintain a reliable estimate. When map data and surrounding vehicle observations were also available, reliable estimation extended to longer ranges as well, showing that the filter handles difficult conditions well when multiple sources are present.

Taken together, the results highlight the value of combining multiple measurement sources for road geometry estimation, where each source contributes complementary information across varying driving conditions, provided that appropriate gating mechanisms are in place to handle unreliable or inconsistent observations.

10.2 Future Work

Several directions could be explored to further improve the proposed method. First, the measurement noise parameters are currently fixed and do not adapt to changing conditions. In practice, measurement quality varies significantly depending on factors such as weather, lighting, and detection range. Adaptive noise tuning, where the measurement noise covariance is adjusted based on the current driving conditions, could therefore improve estimation performance across a wider range of scenarios.

Second, the current formulation assumes that sample points extracted from road features, map data, and vehicle trails are uncorrelated. However, since the road geometry is modeled as a clothoid, consecutive sample points along the road are in reality highly correlated. This assumption is a simplification that may affect filter consistency, and incorporating the true correlation structure into the measurement model could improve both estimation accuracy and the reliability of the NIS consistency checks.

The lane assignment hypotheses currently rely on a uniform prior distribution over all three lanes. A more informative prior could instead be specified based on the road type and the actual number of lanes on the road. This would likely reduce the number of vehicles that are incorrectly rejected during gating as a result of high estimation uncertainty.

Bibliography

[1] I. Sumalatha, P. Chaturvedi, G. R. R, S. Patil, H. P. Thethi, and A. A. Hameed, "Autonomous multi-sensor fusion techniques for environmental perception in self-driving vehicles," in *2024 International Conference on Communication, Computer Sciences and Engineering (IC3SE)*, 2024, pp. 1146–1151. DOI: 10.1109/IC3SE62002.2024.10593125.

[2] J. Kim, D. S. Han, and B. Senouci, "Radar and vision sensor fusion for object detection in autonomous vehicle surroundings," in *2018 Tenth International Conference on Ubiquitous and Future Networks (ICUFN)*, 2018, pp. 76–78. DOI: 10.1109/ICUFN.2018.8436959.

[3] M. Bijelic et al., "Seeing through fog without seeing fog: Deep multimodal sensor fusion in unseen adverse weather," in *2020 IEEE/CVF Conference on Computer Vision and Pattern Recognition (CVPR)*, 2020, pp. 11 679–11 689. DOI: 10.1109/CVPR42600.2020.01170.

[4] Z. Liu et al., "Robust target recognition and tracking of self-driving cars with radar and camera information fusion under severe weather conditions," *IEEE Transactions on Intelligent Transportation Systems*, vol. 23, no. 7, pp. 6640–6653, 2022. DOI: 10.1109/TITS.2021.3059674.

[5] C. Raveena, R. Sravya, R. Kumar, and A. Chavan, "Sensor fusion module using imu and gps sensors for autonomous car," in *2020 IEEE International Conference for Innovation in Technology (INOCON)*, 2020, pp. 1–6. DOI: 10.1109/INOCON50539.2020.9298316.

[6] K. Gupta, A. Singhal, A. Kumar, and P. Maji, "Enhancing sensor perception: Integrating multi-sensor data for robust sensor perception," in *2025 17th International Conference on COMmunication Systems and NETworks (COMSNETS)*, 2025, pp. 78–83. DOI: 10.1109/COMSNETS63942.2025.10885686.

[7] D. Svensson and J. Sörstedt, "Ego lane estimation using vehicle observations and map information," in *2016 IEEE Intelligent Vehicles Symposium (IV)*, 2016, pp. 909–914. DOI: 10.1109/IVS.2016.7535496.

[8] Y.-C. Zhang, "Road geometry estimation using vehicle trails: A linear mixed model approach," *Journal of Intelligent Transportation Systems*, vol. 27, no. 1, pp. 127–144, 2023. DOI: 10.1080/15472450.2021.1974858. eprint: https://doi.org/10.1080/15472450.2021.1974858. [Online]. Available: https://doi.org/10.1080/15472450.2021.1974858.

[9] L. Hammarstrand, M. Fatemi, Á. F. García-Fernández, and L. Svensson, "Long-range road geometry estimation using moving vehicles and roadside observations," *IEEE Transactions on Intelligent Transportation Systems*, vol. 17, no. 8, pp. 2144–2158, 2016. DOI: 10.1109/TITS.2016.2517701.

[10] M. Vázquez-Méndez and G. Casal Urcera, "The clothoid computation: A simple and efficient numerical algorithm," *Journal of Surveying Engineering*, vol. 142, 04016005:1–9, Aug. 2016. DOI: 10.1061/(ASCE)SU.1943-5428.0000177.

[11] H. Marzbani, M. Simic, M. Fard, and R. N. Jazar, "Better road design for autonomous vehicles using clothoids," in *Intelligent Interactive Multimedia Systems and Services*, E. Damiani, R. J. Howlett, L. C. Jain, L. Gallo, and G. De Pietro, Eds., Cham: Springer International Publishing, 2015, pp. 265–278, ISBN: 978-3-319-19830-9.

[12] A. Ahmad, R. Gobithaasan, and J. Ali, "G2 transition curve using quartic bezier curve," Aug. 2007, pp. 223–228. DOI: 10.1109/CGIV.2007.44.

[13] K. Wolhuter, *Geometric Design of Roads Handbook*. Springer, 2015.

[14] E. Bertolazzi and M. Frego, "On the g2 hermite interpolation problem with clothoids," *Journal of Computational and Applied Mathematics*, vol. 341, pp. 99–116, 2018, ISSN: 0377-0427. DOI: https://doi.org/10.1016/j.cam.2018.03.029. [Online]. Available: https://www.sciencedirect.com/science/article/pii/S0377042718301924.

[15] N. Bonnor, "Principles of gnss, inertial, and multisensor integrated navigation systems – second edition paul d. groves artech house, 2013, 776 pp isbn-13: 978-1-60807-005-3," *Journal of Navigation*, vol. 67, pp. 191–192, 2014. [Online]. Available: https://api.semanticscholar.org/CorpusID:112901965.

[16] J.-h. Han, C.-h. Park, c.-k. Hong, and J. Kwon, "Performance analysis of two-dimensional dead reckoning based on vehicle dynamic sensors during gnss outages," *Journal of Sensors*, vol. 2017, pp. 1–13, Sep. 2017. DOI: 10.1155/2017/9802610.

[17] S. Särkkä, *BAYESIAN FILTERING AND SMOOTHING*. Cambridge University Press, 2013.

[18] "Bayesian inference for the multiple linear regression model," in *Introduction to Bayesian Statistics, Third Edition*. John Wiley & Sons, Ltd, 2016, ch. 20, pp. 431–475, ISBN: 9781118593165. DOI: https://doi.org/10.1002/9781118593165.ch19. eprint: https://onlinelibrary.wiley.com/doi/pdf/10.1002/9781118593165.ch19. [Online]. Available: https://onlinelibrary.wiley.com/doi/abs/10.1002/9781118593165.ch19.

[19] S. Särkkä and L. Svensson, "Extended kalman filtering," in *Bayesian Filtering and Smoothing* (Institute of Mathematical Statistics Textbooks), Institute of Mathematical Statistics Textbooks. Cambridge University Press, 2023, pp. 108–130.

[20] H. Arasaratnam and S. Haykin, "Cubature kalman filters," *Automatic Control, IEEE Transactions on*, vol. 54, pp. 1254–1269, Jul. 2009. DOI: 10.1109/TAC.2009.2019800.

[21] Y. Bar-Shalom, X. R. Li, and T. Kirubarajan, *Estimation with Applications to Tracking and Navigation: Theory, Algorithms and Software*. John Wiley & Sons, 2001.

[22] J. Nocedal and S. Wright, *Numerical Optimization*. Springer, 2006.

[23] S. M. Kay, *Fundamentals of Statistical Signal Processing: Estimation Theory*. Prentice Hall, 1993, vol. 1.

[24] D. Simon, *Optimal state estimation: Kalman, H infinity, and nonlinear approaches*. Jan. 2006.

A

NIS Highway Scenario

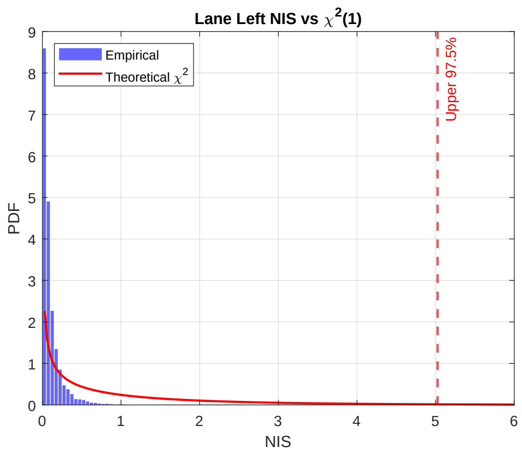

(a) Histogram of NIS values for the left lane markings in the highway log scenario, with the theoretical chi-square distribution and upper-bound threshold.

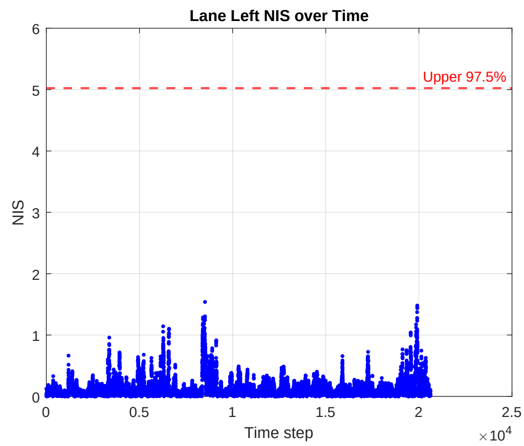

(b) NIS values over time for the left lane markings in the highway log scenario, with the upper-bound threshold.

Figure A.1: Overview of the NIS analysis for the left lane markings.

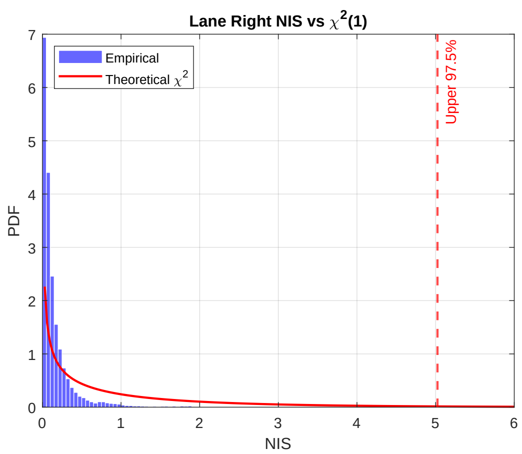

(a) Histogram of NIS values for the right lane markings in the highway log scenario, with the theoretical chi-square distribution and upper-bound threshold.

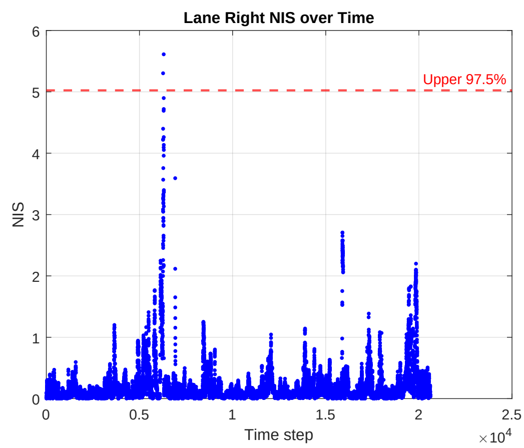

(b) NIS values over time for the right lane markings in the highway log scenario, with the upper-bound threshold.

Figure A.2: Overview of the NIS analysis for the right lane markings.

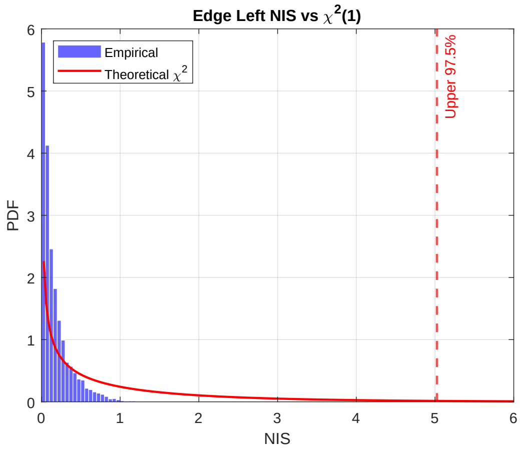

(a) Histogram of NIS values for the left road edges in the highway log scenario, with the theoretical chi-square distribution and upper-bound threshold.

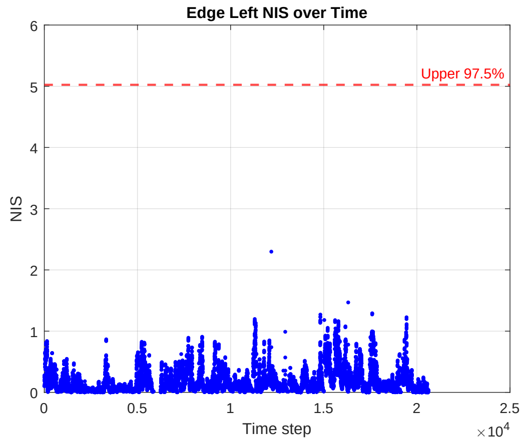

(b) NIS values over time for the left road edges in the highway log scenario, with the upper-bound threshold.

Figure A.3: Overview of the NIS analysis for the left road edges.

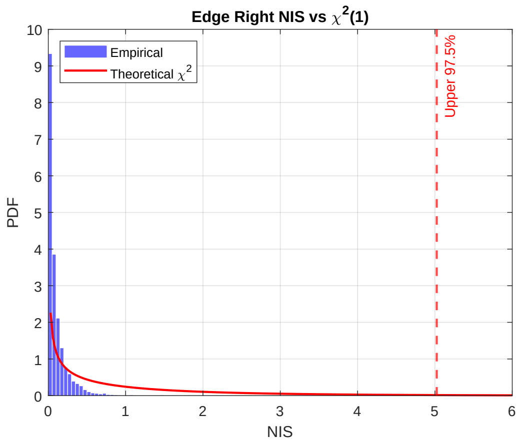

(a) Histogram of NIS values for the right road edges in the highway log scenario, with the theoretical chi-square distribution and upper-bound threshold.

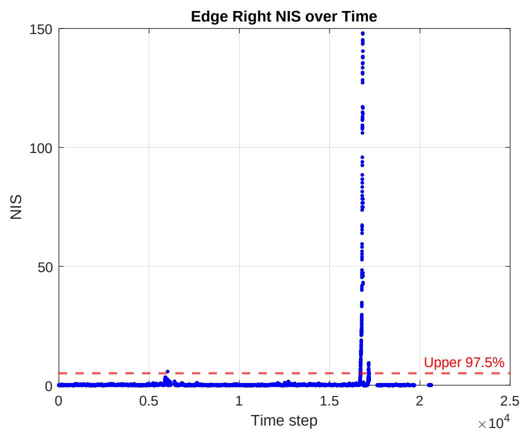

(b) NIS values over time for the right road edges in the highway log scenario, with the upper-bound threshold.

Figure A.4: Overview of the NIS analysis for the right road edges.

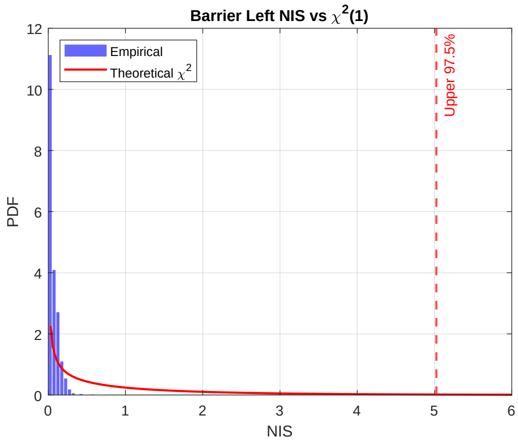

(a) Histogram of NIS values for the left barriers in the highway log scenario, with the theoretical chi-square distribution and upper-bound threshold.

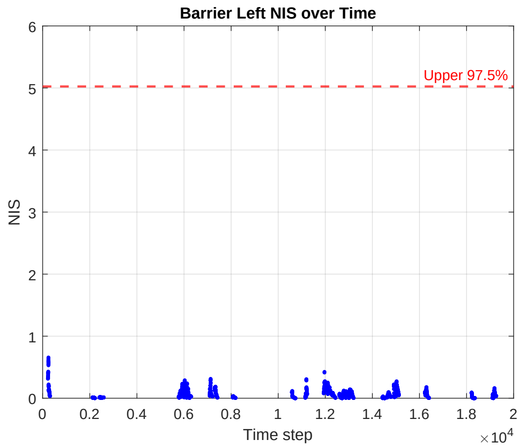

(b) NIS values over time for the left barriers in the highway log scenario, with the upper-bound threshold.

Figure A.5: Overview of the NIS analysis for the left barriers.

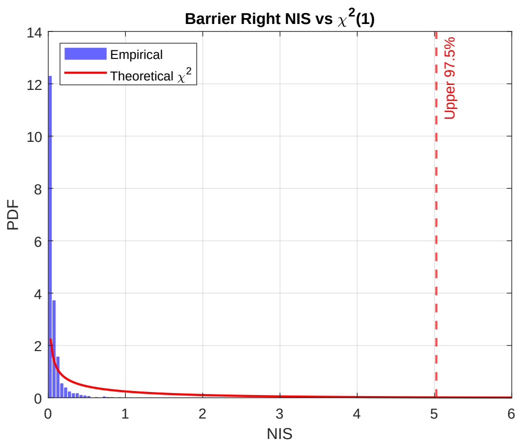

(a) Histogram of NIS values for the right barriers in the highway log scenario, with the theoretical chi-square distribution and upper-bound threshold.

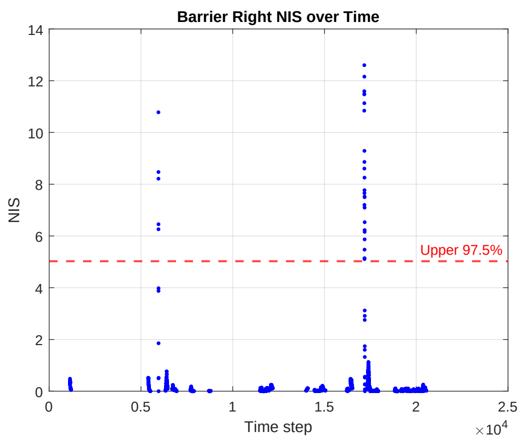

(b) NIS values over time for the right barriers in the highway log scenario, with the upper-bound threshold.

Figure A.6: Overview of the NIS analysis for the right barriers.

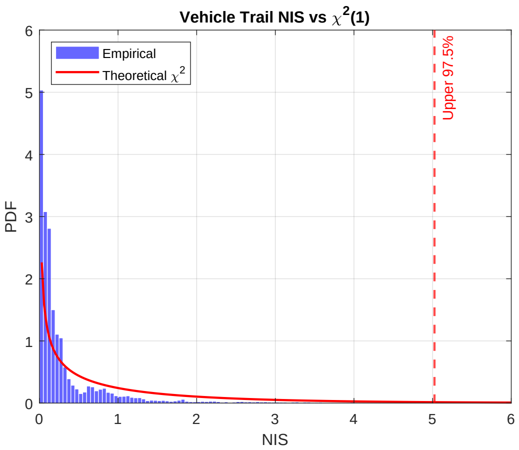

(a) Histogram of NIS values for the vehicle trails in the highway log scenario, with the theoretical chi-square distribution and upper-bound threshold.

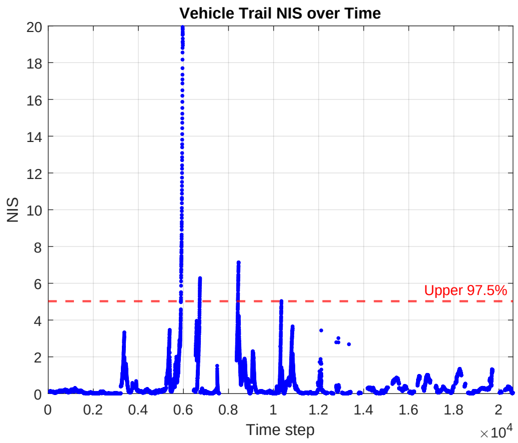

(b) NIS values over time for the vehicle trail in the highway log scenario, with the upper-bound threshold.

Figure A.7: Vehicle Trail NIS

B

NIS for Snow-Covered Rural Scenario 2

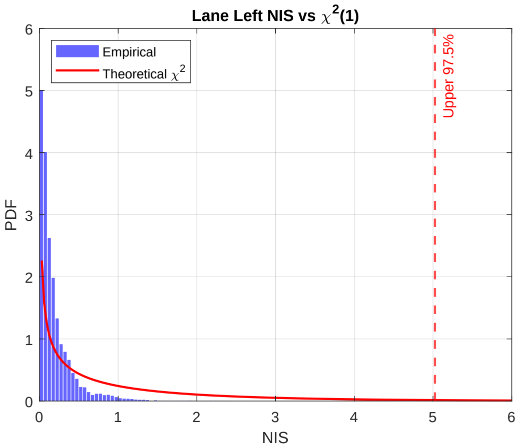

(a) Histogram of NIS values for the left lane markings in the snow-covered rural scenario 2, with the theoretical chi-square distribution and upper-bound threshold.

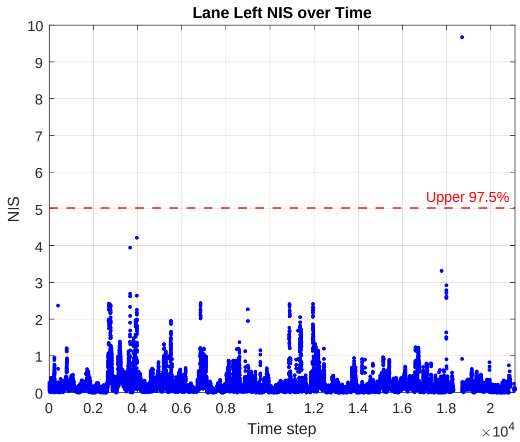

(b) NIS values over time for the left lane markings in the snow-covered rural scenario 2, with the upper-bound threshold.

Figure B.1: Overview of the NIS analysis for the left lane markings.

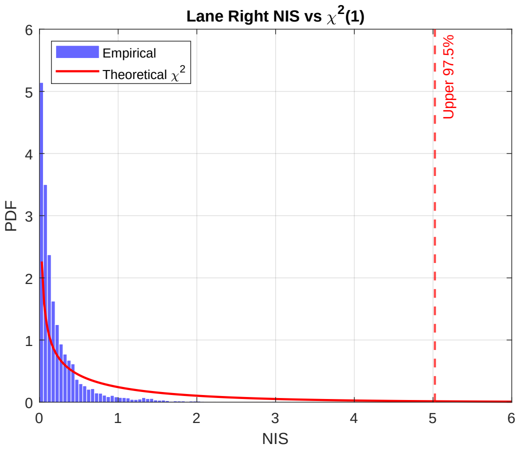

(a) Histogram of NIS values for the right lane markings in the snow-covered rural scenario 2, with the theoretical chi-square distribution and upper-bound threshold.

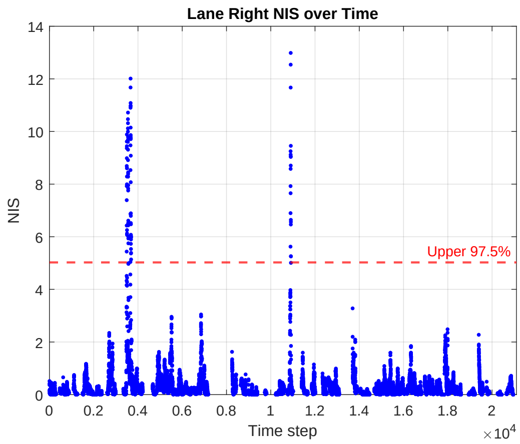

(b) NIS values over time for the right lane markings in the snow-covered rural scenario 2, with the upper-bound threshold.

Figure B.2: Overview of the NIS analysis for the right lane markings.

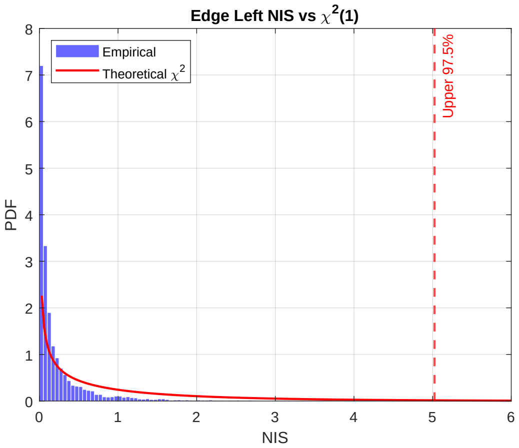

(a) Histogram of NIS values for the left road edges in the snow-covered rural scenario 2, with the theoretical chi-square distribution and upper-bound threshold.

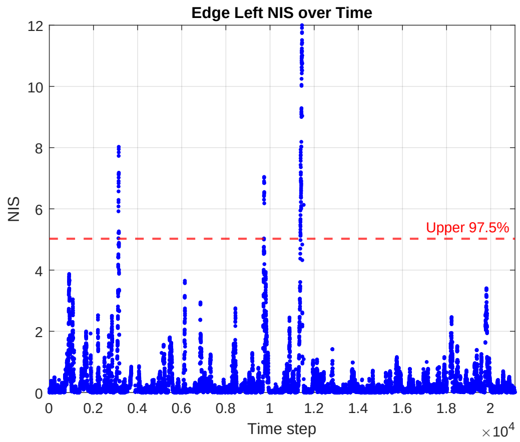

(b) NIS values over time for the left road edges in the snow-covered rural scenario 2, with the upper-bound threshold.

Figure B.3: Overview of the NIS analysis for the left road edges.

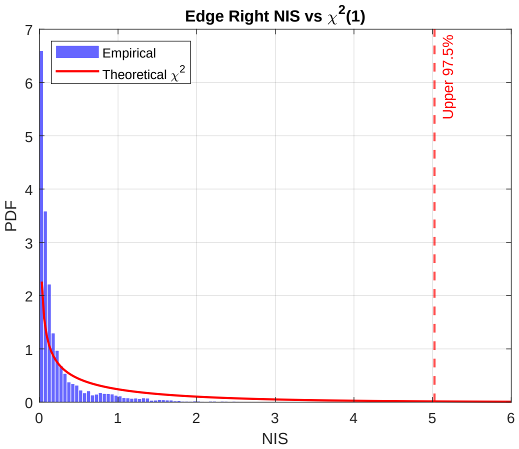

(a) Histogram of NIS values for the right road edges in the snow-covered rural scenario 2, with the theoretical chi-square distribution and upper-bound threshold.

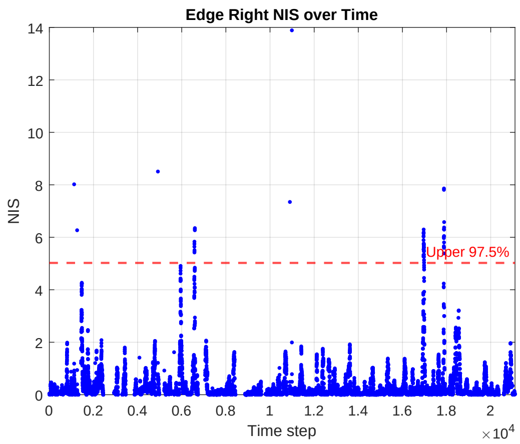

(b) NIS values over time for the right road edges in the snow-covered rural scenario 2, with the upper-bound threshold.

Figure B.4: Overview of the NIS analysis for the right road edges.

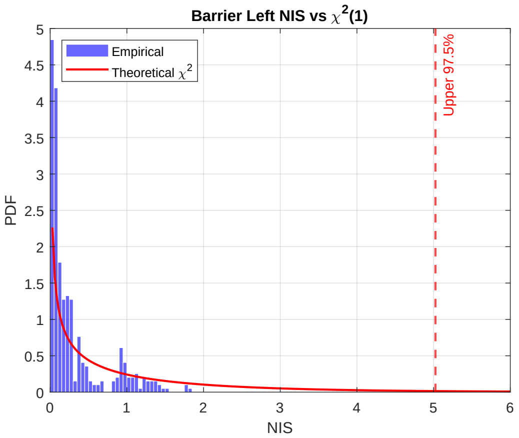

(a) Histogram of NIS values for the left barriers in the snow-covered rural scenario 2, with the theoretical chi-square distribution and upper-bound threshold.

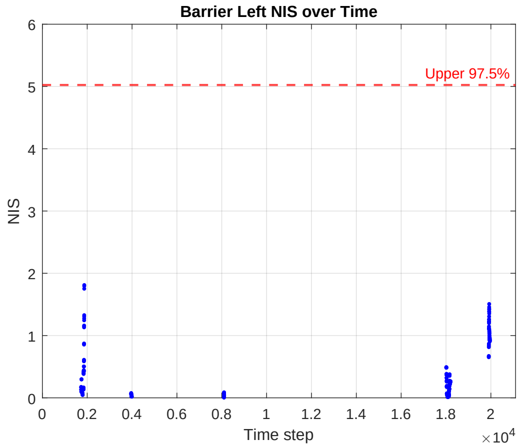

(b) NIS values over time for the left barriers in the snow-covered rural scenario 2, with the upper-bound threshold.

Figure B.5: Overview of the NIS analysis for the left barriers.

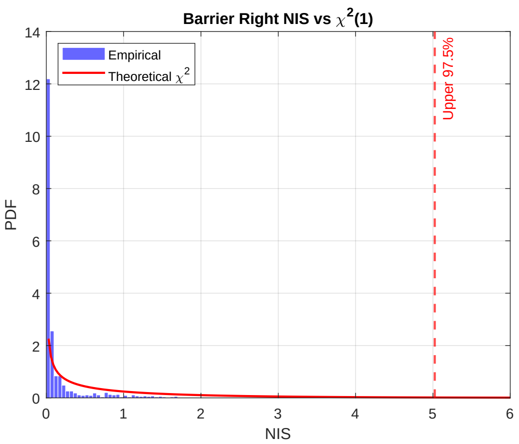

(a) Histogram of NIS values for the right barriers in the snow-covered rural scenario 2, with the theoretical chi-square distribution and upper-bound threshold.

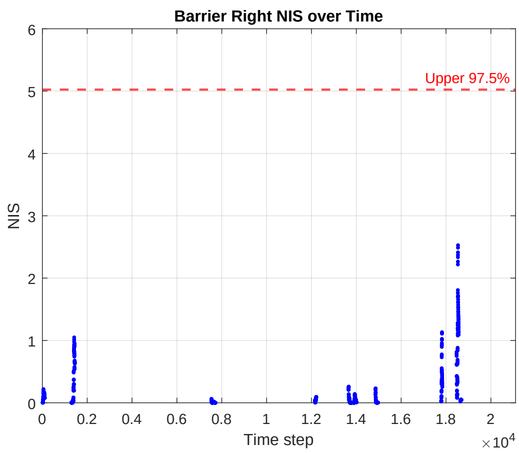

(b) NIS values over time for the right barriers in the snow-covered rural scenario 2, with the upper-bound threshold.

Figure B.6: Overview of the NIS analysis for the right barriers.

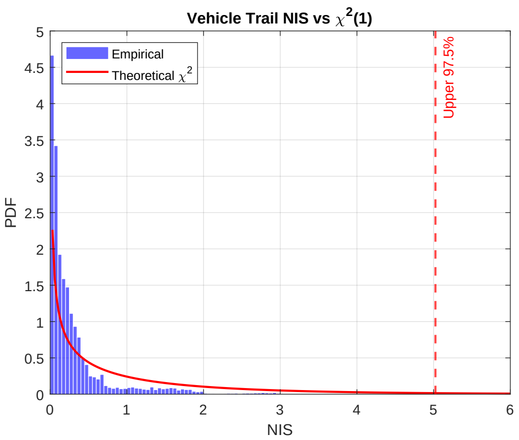

(a) Histogram of NIS values for the vehicle trails in the snow-covered rural scenario 2, with the theoretical chi-square distribution and upper-bound threshold.

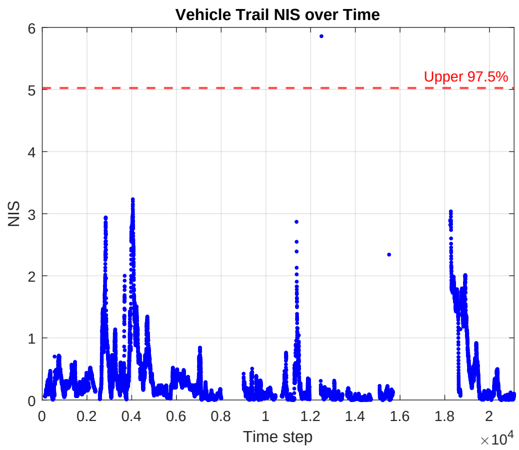

(b) NIS values over time for the vehicle trail in the snow-covered rural scenario 2, with the upper-bound threshold.

Figure B.7: Overview of the NIS analysis for the vehicle trails.

DEPARTMENT OF ELECTRICAL ENGINEERING
CHALMERS UNIVERSITY OF TECHNOLOGY
Gothenburg, Sweden
www.chalmers.se

CHALMERS
UNIVERSITY OF TECHNOLOGY